Ultrafast relaxation of lattice distortion in two-dimensional perovskites

Hao Zhang, Wenbin Li, Joseph Essman, Claudio Quarti, Isaac Metcalf, Wei-Yi Chiang, Siraj Sidhik, Jin Hou, Austin Fehr, Andrew Attar, et al.

To cite this version:

Hao Zhang, Wenbin Li, Joseph Essman, Claudio Quarti, Isaac Metcalf, et al.. Ultrafast relaxation of lattice distortion in two-dimensional perovskites. Nature Physics, 2023, 19 (4), pp.545. 10.1038/s41567-022-01903-6 . hal-03958981

Ultrafast relaxation of lattice distortion in 2D perovskites

Hao Zhang[1,2], Wenbin Li[1,2], Joseph Essman[1], Claudio Quarti[3,4], Isaac Metcalf[5], Wei-Yi Chiang[6], Siraj Sidhik[1,5], Jin Hou[5], Austin Fehr[1], Andrew Attar[7], Ming-Fu Lin[7], Alexander Britz[7], Xiaozhe Shen[7], Stephan Link[6,8], Xijie Wang[7], Uwe Bergmann[9,10], Mercouri G. Kanatzidis[11], Claudine Katan[3], Jacky Even[12], Jean-Christophe Blancon[1]* and Aditya D. Mohite[1]*

[1]Department of Chemical and Biomolecular Engineering, Rice University, Houston, Texas 77005, USA.

[2]Applied Physics Program, Smalley-Curl Institute, Rice University, Houston, TX, 77005, USA.

[3]Univ Rennes, ENSCR, INSA Rennes, CNRS, ISCR (Institut des Sciences Chimiques de Rennes) - UMR 6226, F-35000 Rennes, France.

[4]Laboratory for Chemistry of Novel Materials, Department of Chemistry, University of Mons, Place du Parc 20, 7000 Mons, Belgium

[5]Department of Materials Science and NanoEngineering, Rice University, Houston, TX, 77005, USA.

[6]Department of Chemistry, Rice University, Houston, Texas 77005, USA.

[7]SLAC National Accelerator Laboratory, Menlo Park, CA 94025, USA.

[8]Department of Electrical & Computer Engineering, Rice University, Houston, Texas 77005, USA.

[9]PULSE Institute, SLAC National Accelerator Laboratory, Stanford University, Stanford, CA, USA

[10]Department of Physics, University of Wisconsin–Madison, Madison, WI 53706 USA.

[11]Department of Chemistry, Northwestern University, Evanston, Illinois 60208, USA.

[12]Univ Rennes, CNRS, Institut FOTON (Fonctions Optiques pour les Technologies de l'Information), UMR 6082, CNRS, INSA de Rennes, 35708 Rennes, France.

***Correspondence: blanconjc@gmail.com and adm4@rice.edu**

Direct visualization of ultrafast coupling between charge carriers and lattice degrees of freedom in photo-excited semiconductors has remained a long-standing challenge and is critical for understanding the light-induced physical behavior of materials under extreme non-equilibrium conditions. Here, we obtain a direct visual of the structural dynamics in monocrystalline 2D perovskites. We achieve this by monitoring the evolution of the wave-vector resolved ultrafast electron diffraction intensity following above-bandgap high-density photoexcitation. Our analysis reveals a light-induced ultrafast reduction of antiferro-

distortion resulting from a strong interaction between the electron-hole plasma and the perovskite lattice, which induces an in-plane octahedra rotation towards a more symmetric phase. Correlated ultrafast spectroscopy performed at the same carrier density as ultrafast electron diffraction reveals that the creation of a dense electron-hole plasma triggers the relaxation of lattice distortion at short timescales by modulating the crystal cohesive energy. Finally, we show that the interaction between the carrier gas and the lattice can be altered by tailoring the rigidity of the 2D perovskite by choosing the appropriate organic spacer layer.

Organic-inorganic (hybrid) two-dimensional (2D) halide perovskites (2DP) are constructed by a superlattice of interlocking organic and inorganic nanometer-thick layers and have demonstrated unique and non-classical behaviors and are being extensively explored for a wide range of technologies such as photovoltaics, photodetectors, photocatalysts, light emitting diodes, lasers, and quantum emitters.[1–9] The underlying design principles for each of these devices are strongly correlated to the exact details of how photoexcited or electronically injected charge carriers dissipate their energy via electron-phonon coupling. For example, it has been shown recently, that unusual electron-phonon coupling mechanisms are likely to promote emission of single photons or correlated photon pairs from perovskite quantum sources.[10] There have been only handful experimental studies based on ultrafast or temperature dependent optical spectroscopies to elucidate the carrier dynamics in 2D perovskites. These studies reveal different facets of electron-phonon coupling, which could strongly govern the exciton polaronic effects,[11] hot-carrier dynamics,[12] vibrational relaxation dynamics,[13] and carrier trapping and re-combination rates.[5] Moreover, these measurements also indicate that presence of an organic cation in close proximity to the inorganic perovskite lattice strongly modulates the nature of electron-phonon interactions,[5,11,13–19] and suggest that electron-phonon scattering in 2D perovskites occurs via, local dynamic disorder.[6] These short-range carrier-lattice interactions modulate the quantum-well thickness and octahedral tilts, leading to exciton self-trapping and broadband emission, thanks to the lattice softness, as well as the unique photo-physics properties under extreme non-equilibrium. However, there exists no direct ultrafast structural measurement of 2D perovskites, which elucidates the underlying carrier-lattice interaction mechanisms upon optical excitation. Moreover, the exact geometry and dynamics of these lattice distortions are unknown. This is largely due to the challenges in visualizing the carrier-lattice coupling and dynamics that result after optical excitation above the band-gap.

Here we report the first direct measurement of structural dynamics in 2D perovskites obtained by monitoring the change in the ultrafast femtosecond electron diffraction (UED) after optical excitation. This technique enables a time-resolved structural evolution of the 2D perovskites by tracking the changes in the diffraction pattern, thus providing a direct visualization of lattice response after photo-doping. Detailed analysis of the Bragg peak intensities and temporal signatures reveals an ultrafast reduction of antiferro-distortion at early times ($\tau \leq 1$ ps), which is attributed to the light-induced in-plane rotation of the perovskite octahedra from a distorted to a symmetrical (ordered) phase. Complementary transient absorption measurements further reveal a high excitation regime (beyond Mott transition),[20,21] where a dense electron-hole plasma strongly modulates the crystal cohesive energy,[22] leading to an ultrafast lattice ordering. In parallel, a classical energy transfer to the whole phonon bath via thermal atomic displacements was observed, which was attributed to the Debye-Waller effect. The Debye-Waller effect was associated with a slower rise time ($\tau \sim 5$ps) of the thermal dissipation (or lattice heating). Additionally, the observed long-lived coherent acoustic oscillations suggest the long lifetime of the observed lattice response. Concomitant with the Debye-Waller effect, we also observe an increase in the diffused scattering, which confirms the activation of thermal transfer to the phonon bath. Finally, we show that the mechanism and dynamics of the interaction between the charge carriers and the lattice are acutely tunable and sensitive to the initial lattice distortion of the 2D perovskites dictated by the choice of the organic spacer layer. These findings reveal new and distinct carrier-lattice interactions and counterintuitive mechanisms in 2D perovskites at room temperature, which have not been reported in conventional non-polar/weakly-polar semiconductors such as Si and GaAs or even in 3D iodide perovskites.[23,24]

UED experiment on 2D perovskites

The UED experiments are performed in a pump-probe setup in which sub-micron thick 2D hybrid perovskite single crystals are photoexcited with a 75-fs pulse laser and the structural dynamics are probed with a pulsed electron beam with 150 fs temporal width after specific delay times (t) (Fig. 1a). A diffraction image is acquired at each delay time after above-gap excitation (Fig. 1b), which reflects the instantaneous 2D perovskite crystal structure. Monitoring the characteristics of the diffraction peaks (or Bragg peaks) on the image allows us to directly probe the dynamic changes in the lattice structure after light excitation, revealing the carrier-lattice interactions during energy relaxation (cooling) to the 2D perovskite semiconductors band-edge. We start with a phase-pure (homogenous perovskite layer thickness) 2D perovskite crystal of Dion-Jacobson 4AMP-$MAPb_2I_7$ (DJ n=2) with thickness of 270 nm (Fig. 1a and Fig. S1), which is excited with 3.1 eV light, i.e. 0.9 eV above its ground state optical transition.[25] The diffraction pattern of DJ n=2 at rest is consistent with the static crystal structure reported previously (Fig. 1c and 1d, and details in Fig. S2),[25] which exhibits antiferro-distortions (clockwise and anticlockwise octahedral rotations around the **c** axis) associated with an in-plane doubling of the unit cell (in-plane is defined by **a** and **b** axes).[26,27] The diffraction pattern also indicates that the orientation of the crystal layers is parallel to the substrate (see Supplementary discussion 1 and Fig. S2), with both the light excitation and the probe electron beams impinging along the DJ n=2 stacking axis (**c** axis), as depicted in Fig. 1a.

Fig. 2a shows the differential diffraction map indicating the change in the Bragg peak intensities of the DJ n=2 crystal that occurs within a few picoseconds (t =2 ps, averaged from 1 to 3 ps) after light excitation with a fluence of 2 mJ/cm^2 (corresponds to a carrier density of $2.5\times10^{13}cm^{-2}$, see Supplementary discussion 2). A first visual inspection of this data reveals both an anisotropic response with respect to the in-plane directions in the 2D perovskite lattice and a monotonically decreasing of absolute intensity response with respect to the magnitude of the scattering vector |q|. The Bragg peaks that show a detectable increase in their intensity after light excitation are {400} ((400) and (040)), and {220} (Fig. 2a). The {220} belongs to the {hh0} family and corresponds to the d-spacing of 3.2 Å (Pb-I bonds) along the octahedra diagonal (shown as the highlighted yellow rectangle in Fig. 2b), whereas the {400} Bragg peaks are in the {h00} family correlated with the d-spacing of 2.25 Å (half of octahedron length) along the edge of the octahedra (**a** and **b** directions, shown as cyan in Fig. 2b). On the contrary, higher orders of these two Bragg families such as {800}, {330} and {550}, as well as other directions with reasonable signal ({310}, {530}, {750} and {1020}), all exhibit a decrease in their intensities after photoexcitation. Details of these Bragg peak traces are illustrated in Fig. S3. Furthermore, these transient intensity response scales monotonically with the pump fluence (1mJ/cm^2, estimated carrier density 1.3×10^{13}cm^{-2}), as shown in Fig. S4 for the representative Bragg peaks.

We note that opposite to our results, conventional well-studied bulk semiconductors (such as Si and GaAs), as well as inorganic 2D materials (for example, transition metal dichalcogenides such as MoS_2 and $MoSe_2$), exhibit in most cases a decrease in Bragg peak intensities after photoexcitation.[23,28,29] An increase of Bragg peaks has been reported, resulting from suppression of charge density waves,[30] however no such signatures have been reported in our material system. We also exclude the other unlikely reasons that could induce the Bragg peak increase, based on investigations on temperature-dependent XRD, differential scanning calorimetry, and diffraction modeling from kinematical scattering theory (SI discussion 4). In conventional well-studied materials, the UED signal is attributed to a typical Debye-Waller response, which corresponds to an energy transfer from hot carriers to the low-frequency vibrational density of states, which scale as $|q|^2$.[23,31] A recent study on hybrid three-dimensional (3D) perovskites ($MAPbI_3$) also suggests a Debye-Waller like response, where octahedral rotational disorder induces additional structural deformations.[24] The counterintuitive and opposite behavior of light-induced ordering in some specific crystal directions in DJ n=2 crystals implies that there must exist another competing mechanism, via which the photogenerated carriers strongly interact with the lattice resulting in transient structural change, instead of thermal activation of the phonon bath leading to lattice heating. The increase in the intensities of specific Bragg peaks, thereby counteracting the Debye-Waller effect at short time scale and reducing the lattice distortion (enhanced order) in specific directions.

Mechanism of transient lattice ordering

Qualitative analysis of the diffraction peaks in Fig. 2a suggests that the light-induced transformation may be related to the in-plane lattice reorganization along specific directions. Therefore, we hypothesize that this observed anisotropic lattice ordering originates from the reduction of antiferro-distortions, a specific type of structural deformation involving the rotations of octahedra, which are widely expected in perovskites materials.[9,24,32] To quantify this distortion, we define an order parameter θ as the half of the interlayer Pb-I bonds tilt (Fig. 2b), where θ is around 12° for the intrinsic structural distortion.[25] To test this hypothesis, we reduced the distortions by decreasing the order parameter θ to match the extent of Bragg peak increase in Fig.

2a, and simulated the differential diffraction pattern with respect to the crystal structure in the dark ($\theta_0 = 12^o$, Fig. 2b). The estimated optimal tilt ($\Delta\theta$) is found to be 0.25^o (details of simulation shown in Supplementary discussion 5 and Fig. S5), and the simulated differential diffraction map is shown in Fig. 2c. Compared to the distorted crystal structure at rest, the new structure reduces the adjacent octahedral tilt along the stacking axis (antiferro-distortion), and better aligns the iodine atoms for both octahedral edge {h00} and diagonal directions {hh0}, especially at the distance spacings of Pb-I bonds {220} and half of octahedral edge lengths {400} (yellow and cyan in Fig. 2b). This structural change intensifies the in-plane Bragg peaks including {400} and {220}, consistent with the experimental observations at short time (Fig. 2a). Furthermore, we note that the expected intensity increase is not observed for the higher orders of the Bragg peaks in these two families, such as {800}, {330} and {550}. We attribute this deviation to the combination of both the light-induced reduction of antiferro-distortion (ordering) and the Debye-Waller response. However, because of its $|q|^2$ dependence, the Debye-Waller effect dominates and thus neutralizes the effect of ordering for the higher order Bragg peaks. To quantitively compare these intensity changes, we perform an angular integration at constant |q| of these differential diffraction images (t = 2ps and the simulated one after octahedral re-ordering) (Fig. 2d). The experimental and simulated results are in fair agreement, especially in the low q-value region ($1\ \text{Å}^{-1} < |q| < 3\ \text{Å}^{-1}$) where the Debye-Waller effect is weaker. Therefore, these observations support the hypothesis that the light-induced ultrafast lattice dynamics in DJ n=2, is due to the collective lattice reorganization that reduces the octahedral rotations (Fig. 2b). This hypothesis is further confirmed by our calculations of vibrational modes (SI discussion 5).

Next, in order to gain a deeper insight into the time evolution of the light-induced structural dynamics in 2D hybrid perovskites, we performed a full analysis (up to 100 ps) of the time-dependent intensity changes of the diffraction images after optical excitation. The time traces of the two Bragg peaks {400} and {530} are displayed in Fig. 3a, where the {400} peaks exhibit a significant faster rise-time ($\tau \approx 1$ps, Fig. S3), revealing a diverse response in Bragg peak dynamics besides the intensity change. Furthermore, an overall increase of diffuse scatterings in-between the Bragg peaks spots is visualized, in the differential diffraction images as shown in Fig. 3b. Compared between short-time (t = 2ps) and long-time delays (t = 65ps), the regions in-between the Bragg peaks spots appear redder as most of the Bragg peaks intensifies toward a negative response. The evolution of the integrated diffuse scattering intensities yields an average increase with 0.5% (Fig. S3), suggesting a broad energy transfer process to the phonon bath, along with the Debye Waller effect specified at Bragg peak locations.

To further quantify the different types of lattice dynamics, we fit each Bragg peak intensity curve with a single exponential function, and the fitting details and results are listed in Fig. S3 and Fig. S7, respectively. The maximum positive change (increase in intensity) is 4% and the negative change (decrease in intensity) is 12% (detailed plots in Fig. S3a). The time-constant map (Fig. S7b) shows a clear disparity between the dynamics from different Bragg peak groups. The Bragg peaks with positively changing intensity for which the light-induced lattice ordering mechanism dominates ((400) and (040)), exhibit a very fast time constant of 1 ps or shorter, whereas the peaks with negative intensity response yield a longer time constant on the order of 5 ps. Similar time constants have also been reported in 3D perovskites and have been attributed to the Debye-Waller like response originating from the rotational disorder of the iodine atoms in the perovskite octahedra, leading exclusively to a decrease in peak intensities.[24] A modification of our model including the Debye-Waller effect at long time scale is shown to give a better prediction of intensity changes at large q range than the lattice ordering effect (Fig. S8), confirming the existence of multiple energy transfer processes in 2D perovskites.

All these observations from UED suggest that there are multiple competing mechanisms at play, which attest to the different origins and time scales of carrier-lattice interactions, as illustrated in Fig. 3c. Therefore, we propose that the light-induced lattice ordering, which was attributed to the reduction of the in-plane lattice antiferro-distortion at ultrafast time scale ($\tau \leq 1$ ps), and at longer timescales ($\tau \sim 5$ ps) a Debye-Waller like response.

Lattice transients triggered by dense electron-hole plasma

In order to gain a complete picture of energy transfer and understand the structural dynamics observed in UED measurements, we performed transient absorption (TA) measurements in the same temporal window with similar excitation fluences as the UED experiments on DJ n=2 crystal, (SI discussion 6 and Methods). By monitoring the transmission changes following above-band optical pump et 3.1eV, we estimated the evolution of the effective temperature (T_c) of hot-carrier gas, by fitting the high-energy tail near the band edge with a Maxwell-Boltzmann distribution (analysis details in supplementary discussion 6 and Fig. S11).[33] The hot-carrier dynamics for various fluences are displayed in Fig. 3d. We observe a fast build-up time of the initial carrier temperature within 0.5 ps (Fig. S11b), corresponding to carrier thermalization via carrier-carrier scattering before quasi-equilibrium distribution of hot-carriers, which is typically consistent with the values reported in iodide perovskites.[34] To ensure the carriers reach an effective temperature with quasi-Boltzmann distribution, we perform the analysis of carrier cooling process after 0.5ps. As suggested in Fig. 3d, the evolution of hot carrier distribution reveals a combination of fast (τ ~1ps) and slow (τ ~5ps) cooling processes. This complex carrier cooling behavior is consistent with previous TA report on DJ n=1 perovskite poly-crystalline films (4AMP-PbI_4).[35] The observed fast time scale (sub-ps to 1ps) from both UED and ultrafast spectroscopy may suggest a correlated process that governs the structural change and the carrier response. Furthermore, we attribute the slow cooling process (τ ~5ps) to the typical time of Debye-Waller effect (Fig. 3c), which reflects the relaxation of carrier energy towards the phonon bath and phonon-phonon scatterings, resulting in a lattice heating at similar time scale.

To elucidate the microscopic origin of ultrafast relaxation of lattice distortion, we gave an estimation of the saturated densities (N_{2D}) for both carrier and excitonic responses at different carrier temperatures, as is plotted in Fig. 3e (detailed computation in supplementary discussion 7).[20,36] At a fluence of $1 mJ/cm^2$ in UED experiment, a high electron-hole pair density of $1.3\times10^{13} cm^{-2}$ is generated, with effective temperature of $T_c \approx 3300K$, extrapolated from the carrier temperature in Fig. 3d. This high plasma pair density exceeds the saturation densities for both hot electron-hole plasma (solid line) and cold exciton gas (dashed line, Mott transition density) regimes by one order of magnitude (Fig. 3e). Therefore, we conclude that the observed energy transfer at short time in the UED experiment is rather related to the coupling of a dense carrier plasma to the lattice, instead of exciton polaronic couplings as reported in optical studies on n=1 2D perovskites at low temperature and low excitation fluences.[19]

In the case of a dense electron-hole plasma, strong transient lattice distortions different from Debye-Waller effects can be induced in semiconductors, generating supersonically propagating strain pulses,[37,38] and more complex lattice reorganizations such as the suppression of the ferroelectric instability in $KTaO_3$,[39] and the activation of the antiferro-distorsive rotation of octahedra in $SrTiO_3$.[40] The last case, which was interpreted on the basis of a photodoping-induced modification of the structural soft-mode potential, might be closely related to our present study on

2D perovskites. Furthermore, it was shown that the ultrafast dynamics (τ ~0.2 ps) of the observed antiferro-distortion in $SrTiO_3$ is non-thermally driven by changes of the phonon potential.[40] Thus, we propose a picture where, the electron-hole plasma produces a strong modification of the lattice dielectric properties. On the one hand it results in screening bound electron-hole (exciton) pair formation, and on the other hand modifies the interatomic force constants. This last mechanism of plasma-induced modulation of the interatomic force must be considered because halide perovskites are strongly ionic materials like $SrTiO_3$. The resulting modification of the crystal cohesive energy, manifests as a strong lattice reorganization with antiferro-distortive rotation of octahedra in 2D DJ perovskites. In parallel, a more classical decay of the plasma energy occurs through electron-phonon interactions and observed in structural dynamics associated with a Debye-Waller effect. This classical process is mainly associated with an initial activation of optical phonons, that decay later in time to form acoustic phonons.[35] Additionally, the activation of long-lived acoustic oscillations has been observed from TA measurements (Fig. S12), suggesting a long equilibration time (hundreds of ps) of phonon bath, which is consistent with the long recovery time of the lattice response in UED (Fig. 3a). Such oscillations have been attributed in RP phases to below band gap resonant optical excitation of longitudinal acoustic waves.[41,42] Furthermore, the persistence of the reduction of antiferro-distortion can be attributed to the long-lived electron-hole plasma. Indeed, a high density of carriers persists after reduction of its effective temperature as shown by the long-time bleaching the exciton resonance over 100 to 200ps (Fig. S11f).

Organic cations alter the carrier-lattice interactions

Finally, in order to understand if the mechanism of light-induced transformation is generally applicable to other 2D perovskites with different organic cations and structural phases, we perform UED experiments on three other hybrid 2D perovskites: $4AMP\text{-}MA_2Pb_3I_{10}$ (DJ n=3) exhibiting the same composition as DJ n=2 but a thicker perovskite layer, $BA_2MAPb_2I_7$ (RP n=2) of Ruddlesden-Popper (RP) phase type with same perovskite layer as DJ n=2 but different spacer organic cations (with BA butylammonium), and $BA_2MA_3Pb_4I_{13}$ (RP n=4) with a different perovskite layer and spacer organic cations. The structures of these 2D perovskites are illustrated in Fig. 4a and Fig. 4b, respectively. The experimental UED static diffraction pattern of DJ n=3 (shown in Fig. S13) resembles that of DJ n=2, suggesting that changing the perovskite layer thickness for the DJ 2D perovskites has a negligible effect on the in-plane diffraction pattern.[25]

In order to quantify the different behaviors between the DJ and the RP phase 2D perovskites we evaluated the differential intensity and the time constant of the relevant Bragg peaks. First, we compared the differential intensity between DJ n=2 and DJ n=3 as illustrated in Fig. 4c (detailed diffraction map in Fig. S14), where both samples exhibit similar behaviors. We observed an increase in the intensity of the in-plane Bragg peaks for DJ n=2 {400} and DJ n=3 {040}, and a decrease for the intermediate peaks {310}, {330}, {510} and {530}, consistent with the Debye-Waller effect. These positive changing peaks of DJ crystals exhibit rapid increase with similar time scale of 1ps (Fig. S15). These similarities between the DJ n=2 and n=3 indicate that the phenomena of light-induced ordering at short time scales is generally applicable to the DJ type 2D perovskites. However, in sharp contrast to the DJ case, all the observed Bragg peaks in RP n=2 and n=4 yield a global decrease in intensity (Fig. 4c, detailed time traces and diffraction maps in Fig. S15-S16). Furthermore, comparison of the time constants τ (Fig. 4d, see also SI discussion 3) suggests a generally slower response (up to 15 ps) for RP perovskites than the DJ system. As similarly observed in DJ n=2, an increased diffuse scattering at longer time scales (Fig. S14, Fig. S16 and Fig. S17) indicates a thermal energy transfer to phonon populations, with similar time constant as the Debye-Waller decrease.

These results demonstrate that there is a fundamental difference in the mechanism of carrier-lattice coupling and structural dynamics between the DJ and RP 2D perovskite phases, which implies that the competing mechanism of ultrafast lattice ordering during an antiferro-distortive phase transformation is mitigated in the RP phase. As described in Fig. 4b, the diffraction patterns of RP n=2 and n=4 at rest are consistent with the static crystal structures reported previously, which exhibit almost no antiferro-distortions in plane,[43] contrary to DJ n=2 and n=3 (Fig. 1d and 4a).[25] Therefore, in the RP case the initial ordering step (Fig. 3d) is by-passed and the energy of the hot carriers is directly released to the lattice without the initial energy transfer. We also note that the RP n=4 case is more consistent with the results on 3D $MAPbI_3$, which only shows the Debye-Waller like effect with similar time scales ($\tau \sim 10$ ps).[24] We also note that $MAPbI_3$ indeed exhibit similar intensity variations as RP phases (detailed comparison in SI discussion 8), providing clear evidence of the distinct lattice dynamics in 2D DJ perovskites. These results comparing the nature of carrier-lattice interactions in 2D perovskites with different organic spacer layers provides clear design principle for controlling carrier dynamics in 2D perovskites-based devices.

Acknowledgments

The work at Rice University was supported by start-up funds under the molecular nanotechnology initiative and also the DOE-EERE 2022-1652 program. W.L. acknowledges the National Science Foundation Graduate Research Fellowship Program. This material is based upon work supported by the National Science Foundation Graduate Research Fellowship Program under grant no. NSF 20-587. Any opinions, findings and conclusions or recommendations expressed in this material are those of the author and do not necessarily reflect the views of the National Science Foundation. J.H. acknowledges the financial support from the China Scholarships Council (No. 202107990007). J.Even. acknowledges the financial support from the Institut Universitaire de France. Work at Northwestern was supported by the Office of Naval Research (ONR) under grant N00014-20-1-2725. The experiment was performed at SLAC MeV-UED facility, which is supported in part by the DOE BES SUF Division Accelerator & Detector R&D program, the LCLS Facility, and SLAC under contract Nos. DE-AC02-05-CH11231 and DE-AC02-76SF00515. S.L. thanks the Robert A. Welch Foundation for support through the Charles W. Duncan, Jr.-Welch Chair in Chemistry (C-0002), and acknowledges financial support from the U.S. Department of Energy, Office of Science, Basic Energy Sciences, CPIMS Program, under Award # DE-339SC0016534, which for this work supported W.-Y. C.

Author contributions

A.D.M. and J-C. B. conceived and designed the experiment. J.H. and S.S. synthesized the perovskite single crystals, and W.L. prepared samples with the help of J.H. and H.Z; H.Z. performed optical absorbance characterizations. W.L., H.Z., S.S. and A.F. performed the UED experiments with the help of. A.A, M.-F.L, A.B., X.Z., X.W. and U.B.; H.Z. performed data analysis under the help of J.Essman and I.M, with guidance from J.-C.B., J.Even. and M.G.K. Phonon modeling was carried out by C.Q. with guidance from J. Even and C.K.; W.Y. performed TA measurements with guidance from S.L. J.-C. B. and A. D. M. wrote the manuscript with inputs from everyone. All authors read the manuscript and agree to its contents, and all data are reported in the main text and supplemental materials.

Competing Interests

The authors declare no competing interests.

Figure Legends/Captions

Fig. 1 | UED measurements on 4AMP-MAPb$_2$I$_7$ (DJ n=2) 2D perovskite. a, Schematics of UED apparatus. The directions of light pump and electron probe with respect to crystal orientation is illustrated. (inset) Optical microscopic top-view image of DJ n=2 single crystal. The dashed yellow line idicates the transmission window for the electron beam. Scale bar is 50μm. **b,** Electron diffraction pattern of DJ n=2 crystal at different pump-probe delay time: t = 0 ps, 1 ps and 35 ps. **c,** Static diffraction pattern ($t \leq 0$) and indexing of Bragg planes (hk0). Diffraction peaks circled with white, brown, cyan, green, and yellow colors belong to {200}, {110}, {400}, {310}, and {220} Bragg peak families, respectively. The diffraction peaks {110} are partially blocked by the direct beam filter ($q<1\text{Å}^{-1}$). **d,** Crystal structure of DJ n=2 viewing at [110] and [001] directions, showing intrinsic antiferro-distortion (in-plane octahedral rotations). The corresponding Bragg plane directions are displayed for {400} (cyan),{310} (green) and {220} (yellow).

Fig. 2 | Reduction of lattice distortion observed from UED response of DJ n=2 crystal. a, Differential diffraction map at t=2 (±1) ps, acquired by subtracting the averaged response of $1-3$ ps after light excitation by the response at rest ($t \leq 0$ ps). The intensity change ΔI (increase and decrease) of each specific Bragg peak (hk0) is indicated by red and blue colors, respectively. The map is zoomed in to the first quadrant ($0<q_x$, $q_y<6\text{Å}^{-1}$). **b,** Crystal structure at rest showing intrinsic antiferro-distortion (top) and simulated structure reducing the distortion (bottom), with order parameter θ defined as half of the interlayer octahedral rotations. For clarity the organic cations are omitted. **c,** Simulated differential diffraction map between the two crystal structures in Fig. 2b, showing intensity change (ΔI) of each Bragg peak after reducing the antiferro-distortion angle θ. **d,** Angular-integrated differential diffraction (filtering out diffuse scattering regions), comparing the experimental data (t=2 (±1) ps) (gray solid line and shadow), the expected Debye-Waller response (gray dashed line), and simulated signal acquired from Fig. 2c (black solid line). Note that the {110} peaks are partially filtered by the direct beam blocker (Fig. 1c).

Fig. 3 | Lattice (in-plane) and carrier response of DJ n=2 crystal under light excitation. a, Intensity dynamic plots of peak families {400} and {530}. **b,** 2D differential diffraction map averaged at t = 2ps (left half) and t = 65ps (right half), with blue for intensity decrease and red for increase. The dashed region indicates the area with the most increase of diffuse scatterings. **c,** Schematics of light-induced reduction of antiferro-distortion and thermally activated atomic displacement from Debye-Waller effect. **d**, Evolution of carrier temperatures (T_c) as a function of delay times at different excitation densities (1.1, 3.4, 5.6 and 8.4×10^{12} cm^{-2}), showing fast and slow cooling processes. **e**, Estimation of saturation densities (N_{2D}) for DJ n=2 (red) and RP n=2 (blue) crystals at different temperatures. The saturation densities due to electron-hole plasma and exciton gas are shown in solid and dashed lines, respectively. For 1mJ/cm^2, a hot e-h plasma is generated (1.3×10^{13} cm^{-2}), as indicated by the gray dashed arrow.

Fig. 4 | Comparison between different 2D perovskite structures with different organic cations. Crystal structures of the **a,** DJ n=3 and **b,** RP n=2 and n=4 perovskites. **c,** Angular integrated differential diffraction plot (20 − 40ps) for the DJ n=2, DJ n=3, RP n=2 and RP n=4 perovskites. The yellow and cyan colors label the Bragg peaks showing positive responses in DJ systems. **d,** Histogram of rise-time constants of DJ n=2, DJ n=3 and RP n=4 structures.

References

1. Tsai, H. *et al*. High-efficiency two-dimensional Ruddlesden–Popper perovskite solar cells. *Nature* **536**, 312–316 (2016).
2. Li, L. *et al*. Tailored engineering of an unusual (C4H9NH3) 2 (CH3NH3) 2Pb3Br10 two-dimensional multilayered perovskite ferroelectric for a high-performance photodetector. *Angewandte Chemie* **129**, 12318–12322 (2017).
3. Yuan, M. *et al*. Perovskite energy funnels for efficient light-emitting diodes. *Nature Nanotechnology* **11**, 872–877 (2016).
4. Qin, C. *et al*. Stable room-temperature continuous-wave lasing in quasi-2D perovskite films. *Nature* **585**, 53–57 (2020).
5. Gong, X. *et al*. Electron–phonon interaction in efficient perovskite blue emitters. *Nature Materials* **17**, 550–556 (2018).
6. Blancon, J.-C., Even, J., Stoumpos, C. C., Kanatzidis, M. G. & Mohite, A. D. Semiconductor physics of organic–inorganic 2D halide perovskites. *Nature Nanotechnology* **15**, 969–985 (2020).
7. Kepenekian, M. *et al*. Concept of Lattice Mismatch and Emergence of Surface States in Two-dimensional Hybrid Perovskite Quantum Wells. *Nano Lett*. **18**, 5603–5609 (2018).

8. Blancon, J.-C. *et al*. Extremely efficient internal exciton dissociation through edge states in layered 2D perovskites. *Science* **355**, 1288–1292 (2017).

9. Smith, M. D., Jaffe, A., Dohner, E. R., Lindenberg, A. M. & Karunadasa, H. I. Structural origins of broadband emission from layered Pb–Br hybrid perovskites. *Chem. Sci.* **8**, 4497–4504 (2017).

10. Tamarat, P. *et al*. The dark exciton ground state promotes photon-pair emission in individual perovskite nanocrystals. *Nat Commun* **11**, 6001 (2020).

11. Neutzner, S. *et al*. Exciton-polaron spectral structures in two-dimensional hybrid lead-halide perovskites. *Phys. Rev. Materials* **2**, 064605 (2018).

12. Yin, J. *et al*. Tuning Hot Carrier Cooling Dynamics by Dielectric Confinement in Two-Dimensional Hybrid Perovskite Crystals. *ACS Nano* **13**, 12621–12629 (2019).

13. Quan, L. N. *et al*. Vibrational relaxation dynamics in layered perovskite quantum wells. *PNAS* **118**, e2104425118 (2021).

14. Guo, Z., Wu, X., Zhu, T., Zhu, X. & Huang, L. Electron–Phonon Scattering in Atomically Thin 2D Perovskites. *ACS Nano* **10**, 9992–9998 (2016).

15. Jia, X. *et al*. Observation of enhanced hot phonon bottleneck effect in 2D perovskites. *Appl. Phys. Lett.* **112**, 143903 (2018).

16. Straus, D. B. *et al*. Direct Observation of Electron–Phonon Coupling and Slow Vibrational Relaxation in Organic–Inorganic Hybrid Perovskites. *J. Am. Chem. Soc.* **138**, 13798–13801 (2016).

17. Ni, L. *et al*. Real-Time Observation of Exciton–Phonon Coupling Dynamics in Self-Assembled Hybrid Perovskite Quantum Wells. *ACS Nano* **11**, 10834–10843 (2017).

18. Guo, P. *et al*. Direct Observation of Bandgap Oscillations Induced by Optical Phonons in Hybrid Lead Iodide Perovskites. *Advanced Functional Materials* **30**, 1907982 (2020).

19. Thouin, F. *et al*. Phonon coherences reveal the polaronic character of excitons in two-dimensional lead halide perovskites. *Nature Materials* **18**, 349–356 (2019).

20. Schmitt-Rink, S., Chemla, D. S. & Miller, D. A. B. Theory of transient excitonic optical nonlinearities in semiconductor quantum-well structures. *Phys. Rev. B* **32**, 6601–6609 (1985).

21. Chemla, D. S. & Miller, D. a. B. Room-temperature excitonic nonlinear-optical effects in semiconductor quantum-well structures. *J. Opt. Soc. Am. B, JOSAB* **2**, 1155–1173 (1985).

22. Stampfli, P. & Bennemann, K. H. Time dependence of the laser-induced femtosecond lattice instability of Si and GaAs: Role of longitudinal optical distortions. *Phys. Rev. B* **49**, 7299–7305 (1994).

23. Harb, M. *et al*. Carrier Relaxation and Lattice Heating Dynamics in Silicon Revealed by Femtosecond Electron Diffraction. *J. Phys. Chem. B* **110**, 25308–25313 (2006).

24. Wu, X. *et al*. Light-induced picosecond rotational disordering of the inorganic sublattice in hybrid perovskites. *Science Advances* **3**, e1602388 (2017).

25. Mao, L. *et al*. Hybrid Dion–Jacobson 2D Lead Iodide Perovskites. *J. Am. Chem. Soc.* **140**, 3775–3783 (2018).

26. Kepenekian, M. *et al*. Rashba and Dresselhaus effects in hybrid organic–inorganic perovskites: from basics to devices. *ACS nano* **9**, 11557–11567 (2015).

27. Even, J., Carignano, M. & Katan, C. Molecular disorder and translation/rotation coupling in the plastic crystal phase of hybrid perovskites. *Nanoscale* **8**, 6222–6236 (2016).

28. Lin, M.-F. *et al*. Ultrafast non-radiative dynamics of atomically thin MoSe 2. *Nature Communications* **8**, 1745 (2017).

29. Mannebach, E. M. *et al*. Dynamic Structural Response and Deformations of Monolayer MoS2 Visualized by Femtosecond Electron Diffraction. *Nano Lett.* **15**, 6889–6895 (2015).

30. Erasmus, N. *et al*. Ultrafast Dynamics of Charge Density Waves in `$4{H}_{b}\mathrm{\text{\ensuremath{-}}}{\mathrm{TaSe}}_{2}$` Probed by Femtosecond Electron Diffraction. *Phys. Rev. Lett.* **109**, 167402 (2012).

31. Harb, M. *et al*. Phonon-phonon interactions in photoexcited graphite studied by ultrafast electron diffraction. *Phys. Rev. B* **93**, 104104 (2016).

32. Cortecchia, D. *et al*. Broadband Emission in Two-Dimensional Hybrid Perovskites: The Role of Structural Deformation. *J. Am. Chem. Soc.* **139**, 39–42 (2017).

33. Yang, Y. *et al*. Observation of a hot-phonon bottleneck in lead-iodide perovskites. *Nature Photonics* **10**, 53–59 (2016).

34. Richter, J. M. *et al*. Ultrafast carrier thermalization in lead iodide perovskite probed with two-dimensional electronic spectroscopy. *Nature Communications* **8**, 376 (2017).

35. Yin, J. *et al*. Manipulation of hot carrier cooling dynamics in two-dimensional Dion–Jacobson hybrid perovskites via Rashba band splitting. *Nat Commun* **12**, 3995 (2021).

36. Blancon, J.-C. *et al*. Scaling law for excitons in 2D perovskite quantum wells. *Nature Communications* **9**, 2254 (2018).

37. DeCamp, M. F. *et al*. Transient Strain Driven by a Dense Electron-Hole Plasma. *Phys. Rev. Lett.* **91**, 165502 (2003).

38. Young, E. S. K., Akimov, A. V., Campion, R. P., Kent, A. J. & Gusev, V. Picosecond strain pulses generated by a supersonically expanding electron-hole plasma in GaAs. *Phys. Rev. B* **86**, 155207 (2012).

39. Krapivin, V. *et al*. Ultrafast Suppression of the Ferroelectric Instability in ${\mathrm{KTaO}}_{3}$. *Phys. Rev. Lett.* **129**, 127601 (2022).

40. Porer, M. *et al*. Ultrafast Relaxation Dynamics of the Antiferrodistortive Phase in Ca Doped ${\mathrm{SrTiO}}_{3}$. *Phys. Rev. Lett.* **121**, 055701 (2018).

41. Guo, P. *et al*. Cross-plane coherent acoustic phonons in two-dimensional organic-inorganic hybrid perovskites. *Nature Communications* **9**, 2019 (2018).

42. Maity, P. *et al*. Layer-Dependent Coherent Acoustic Phonons in Two-Dimensional Ruddlesden–Popper Perovskite Crystals. *J. Phys. Chem. Lett.* **10**, 5259–5264 (2019).

43. Stoumpos, C. C. *et al*. Ruddlesden–Popper Hybrid Lead Iodide Perovskite 2D Homologous Semiconductors. *Chem. Mater.* **28**, 2852–2867 (2016).

44. Dovesi, R. *et al*. Quantum-mechanical condensed matter simulations with CRYSTAL. *Wiley Interdisciplinary Reviews: Computational Molecular Science* **8**, e1360 (2018).

45. Jp, P., K, B. & M, E. Generalized Gradient Approximation Made Simple. *Phys Rev Lett* **77**, 3865–3868 (1996).
46. Grimme, S., Antony, J., Ehrlich, S. & Krieg, H. A consistent and accurate ab initio parametrization of density functional dispersion correction (DFT-D) for the 94 elements H-Pu. *J. Chem. Phys.* **132**, 154104 (2010).
47. Ivanovska, T. *et al*. Vibrational Response of Methylammonium Lead Iodide: From Cation Dynamics to Phonon–Phonon Interactions. *ChemSusChem* **9**, 2994–3004 (2016).
48. Monkhorst, H. J. & Pack, J. D. Special points for Brillouin-zone integrations. *Phys. Rev. B* **13**, 5188–5192 (1976).
49. Pascale, F. *et al*. The calculation of the vibrational frequencies of crystalline compounds and its implementation in the CRYSTAL code. *Journal of Computational Chemistry* **25**, 888–897 (2004).

Methods

Materials

The materials used for 2D perovskites (DJ and RP) precursors were purchased from Sigma Aldrich, including methylamine hydrochloride (MACl), lead oxide (PbO), 4-aminomethyl piperidine (4AMP), butylamine (BA), hypophosphorous acid (H_3PO_2), and hydroiodic (HI). Methylamine iodide (MAI) was purchased from Greatcell Solar.

Single crystal synthesis and transfer

Single Crystal Synthesis: BA n=2,4 perovskites solution was synthesized by adopting the previously reported procedure, using 0.4 times the scale.[25] 4AMP n=2,3 perovskites solution was synthesized by adopting the previously reported procedure, using 0.5 times the scale.[43] Glass was used as the substrate for the 2D perovskite growth. Glass substrates were cut into 2.5 cm × 2.5 cm squares, then cleaned in soapy water, isopropanol, and acetone by ultrasonication for 20 min each, and then were dried using an argon gun. The substrates were transferred into a UV-Ozone cleaner, and cleaned for 20 min. 10 μL of the diluted solution was deposited dropwise onto the glass surface. Another glass was put on top to fully cover the bottom glass and dried overnight at 80 °C for BA and 75 °C for 4AMP. A thin single crystal grew spontaneously as the solvent evaporated.

Crystal Exfoliation and Transfer: Large-flake single-crystal perovskites were mechanically exfoliated and then transferred onto 100 × 100μm TEM transmission windows with silicon nitride membranes. All samples were prepared and sealed in Argon gas until UED measurements. A comparison of diffraction images between first and last scans suggests no new peaks arising, confirming no degradation during the measurement period (Fig. S19).

Sample characterization

Optical absorbance: The optical absorbance of the single crystals was determined based on confocal microscopy, by focusing a broad-spectrum white light beam (Thorlabs SOLIS-3C) into a 50um spot and measuring the transmission spectrum through a TEM window. The spectrum was acquired using a spectrometer (Andor Kymera 328i) and CCD (Andor iDus 416).

Differential scanning calorimetry (DSC): Differential scanning calorimetry was performed from room temperature to 150℃ with a ramp rate of 15℃/min. The heat capacity of the sample was calculated from the heat flow (W/g) and was calibrated using a sapphire sample as a reference.

Ultrafast electron diffraction (UED)

UED experiments were performed at SLAC National Accelerator Laboratory. Electrons were accelerated to 3.7 MeV by Klystron with temporal width of 150fs. Normal incident pulses were diffracted by the sample in transmission geometry on TEM transmission window, and diffracted intensities were captured by an EMCCD. The electron pules were synchronized with a laser beam (3.1eV, $\tau_{\mathrm{width}} \approx 75$fs) at the frequency of 180Hz, with temporal delay typically from -20ps to 100ps. The delay time was tuned by adjusting the relative path length difference using a delay stage. To reduce the confounding effect of mechanical shift and possible crystal structural change during time evolution ($T_{\mathrm{total}} \sim$ hrs.), the sequence of stage locations was configured randomly during each scan. Each typical UED run contained $20 - 30$ pump-probe scans and each diffraction image was averaged over approximately 8000 shots to reduce statistical fluctuations.

UED Bragg peaks indexing: The Bragg peaks of the measured samples (DJ n=2, DJ n=3, RP n=2 and RP n=4) were indexed by comparing the diffraction patterns with the simulated diffraction images calculated via SingleCrystal software (http://crystalmaker.com/singlecrystal/), using structure files (.cif) from Mao et al.[25] These comparisons are shown in Fig. S2 (DJ n=2), Fig. S13 (DJ n=3), Fig. S20 (RP n=2) and Fig. S21 (RP n=4).

UED data processing: A stack of diffraction maps at different time steps was collected for each sample measurement. Each diffraction image was background-removed by CCD dark counts and normalized by total diffraction intensity. To extract the time traces of relative intensity response of each Bragg peak ($\Delta I(t)/I_0$), we first integrated the intensity within a ROI centered at each peak (0.2Å in diameter), and then normalized the intensity curve by averaging over negative delays (t<0). Time traces of Bragg peaks were fitted globally by a single exponential curve:

$$\Delta I(t)/I_0 = \begin{cases} 0 & , \ t < t_0 \\ \Delta\left(\exp\left(\frac{t-t_0}{\tau}\right) - 1\right), & t \geq t_0 \end{cases}$$

Where Δ stands for intensity change (%), τ for time constant (ps), and t_0 for time zero offset (calibrated by the response of bismuth crystal and fixed globally). Fitting results are plotted in Fig. S7 (DJ n=2) and Fig. S18 (DJ n=3 and RP n=4). Results of selected peak families of DJ n=2 are displayed in Fig. S3. Error intervals of the fitting parameters Δ and τ were estimated from one standard deviation calculated from the square root of the covariance matrix diagonal. Fitting methods were based on least squares optimization performed by 'curve_fitting' function using Python (version 3.7.4).

Transient absorption spectroscopy (TA)

Transient absorption (TA) experiments for 2D perovskites were done by using a 400 nm pump beam and a supercontinuum white light probe beam ranging from 450 to 750 nm. The pump laser was obtained from a 2nd harmonic generator (Ultrafast System) derived by a fundamental 60 fs-pulsed laser (Coherent, Inc.) at 800 nm with a repetition rate of 1 kHz. The 1 kHz pump laser passed through a chopper to yield a 500 Hz modulation frequency. The pump fluence was controlled within 0.1 − 0.75 mJ/cm^2. The supercontinuum white light laser was generated by introducing the fundamental laser into a nonlinear crystal, CaF2 (Ultrafast System). Pump and probe beam pulses were temporally and spatially overlapped and focused on the 2D perovskites.

2D perovskites were measured in ambient air condition with DJ n=2 sample sealed with 50nm thick PMMA on top.

Phonon simulation methods

Phonon modes simulation: These simulations were based on periodic Density Functional Theory (DFT) calculations, performed within Linear Combination of Atomic Orbital (LCAO) formalism, as implemented in the CRYSTAL17 code.[44] Electronic ground state was computed within the GGA approximation, employing the PBE exchange-correlation functional,[45] along with double split basis set quality and core potentials for heavy Pb and I atoms. Dispersion D3 scheme was included to account for van-der Waals interactions,[46] as these are expected to play an important role in the packing of the organic component. As it is not currently implemented in CRYSTAL17, Spin-Orbit-Coupling (SOC) has been neglected in the present calculations. Nevertheless, SOC is not expected to heavily affect the ion dynamics, with current computational set-up providing vibrational frequencies in nice agreement with experimental data, for the reference orthorhombic phase of the 3D methylammonium lead iodide perovskite.[47]

Calculations have been performed on the reference crystalline structure of the DJ n=2 system from Ref.[25], adopting 2x4x4 sampling of the first Brillouin zone, in the Monkhorst-Pack scheme[48] (with the less dense sampling associated to the longer plane-stacking direction). Crystalline structure was fully relaxed with only constraint related to the native space group symmetry (Cc n°9). The hessian was estimated at the Γ point of the Brillouin zone, via finite displacements,[49] resulting in zero negative frequencies. Resulting normal modes were used as special coordinates along which to distort the crystal structure and to evaluate the change in the electron diffraction pattern, as exemplified in Fig. S6. These calculations reveal that antiferro-distortive phonon modes associated with the octahedra rotations are indeed predicted for the crystal structure at rest, thus further confirmed our hypothesis on lattice ordering via reduction of antiferro-distortion (Fig. 2).

Electron diffraction simulation: Snapshots of the crystalline structure as distorted along all the computed normal modes were then provided as crystallographic information files (.cif) and used to simulate electron diffraction intensities using SingleCrystal software. The simulated 2D patterns and 1D azimuthally integrated plots were reconstructed by convolving the localized Bragg peaks with gaussian shape with FWHM of 0.17Å.

Data availability

All the data supporting the findings of this study are available and are attached. Any additional data are available from the authors upon reasonable request.

Code availability

The analysis code for this study is available from the authors upon reasonable request.

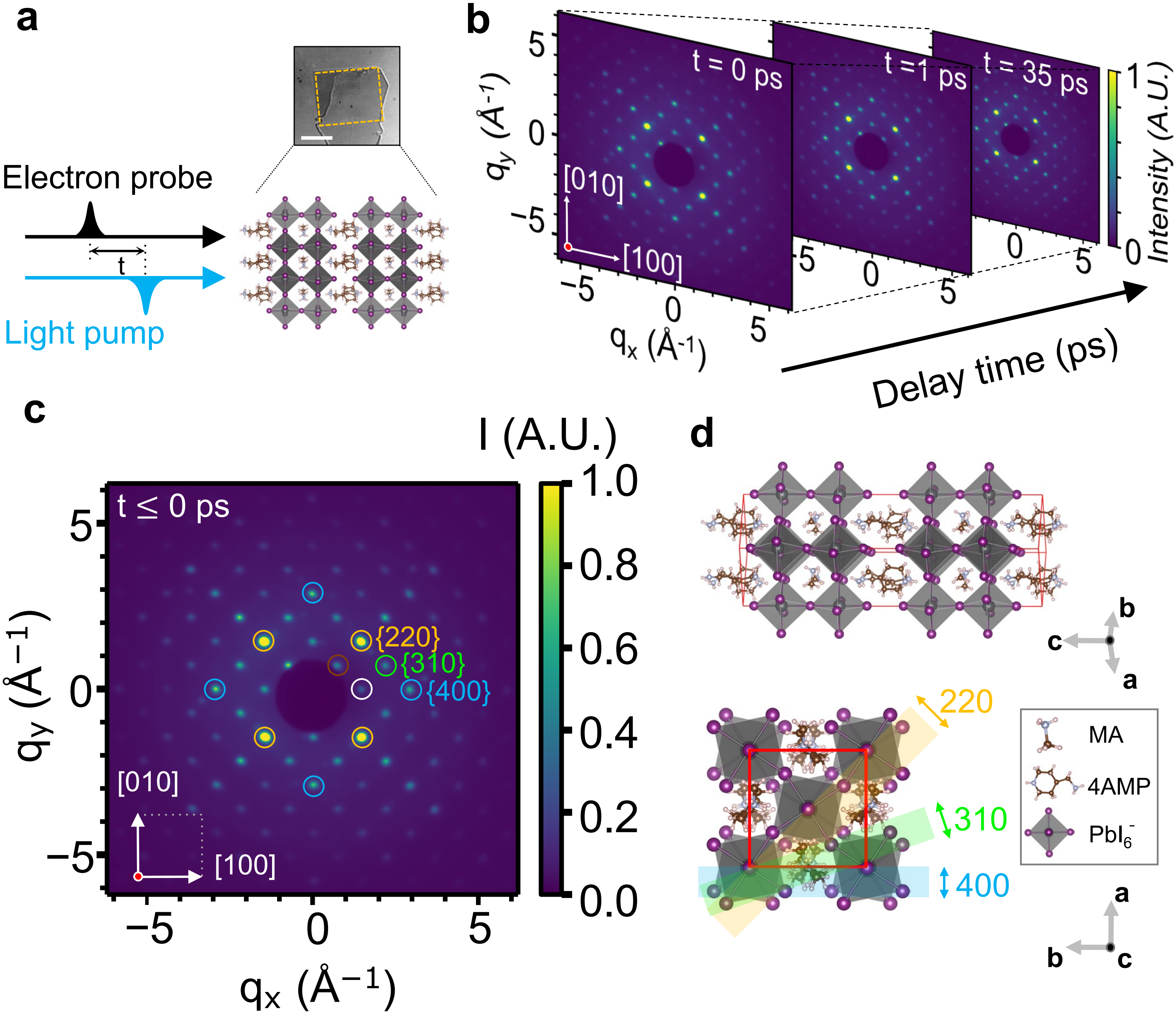
a
Electron probe
t
Light pump
b
t = 0 ps
t =1 ps
t = 35 ps
q_y (Å-1)
q_x (Å-1)
[010]
[100]
Intensity (A.U.)
Delay time (ps)
c
t ≤ 0 ps
I (A.U.)
{220}
{310}
{400}
[010]
[100]
q_y (Å−1)
q_x (Å−1)
d
220
310
400
MA
4AMP
PbI6-
a
b
c

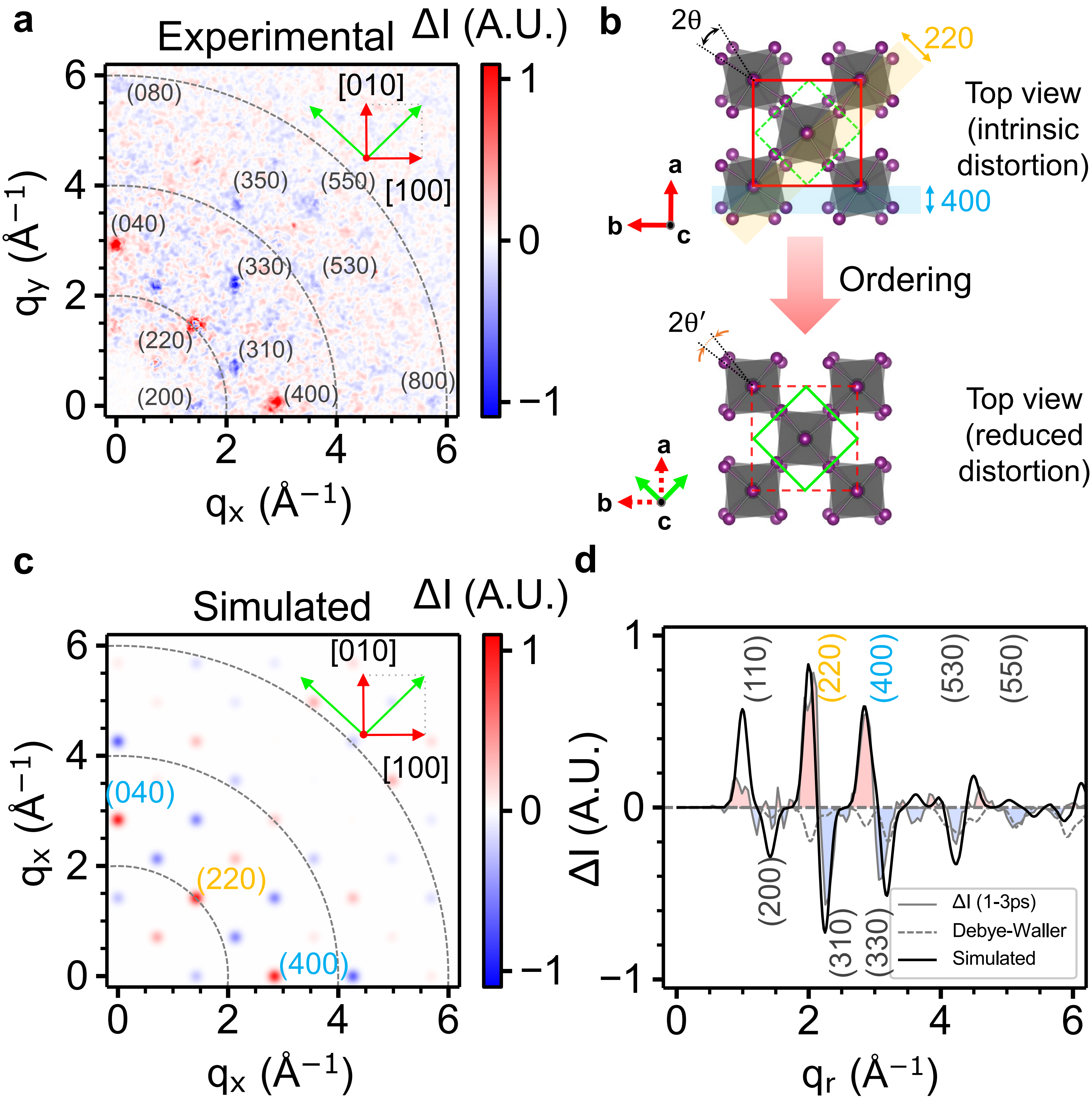
a
Experimental
ΔI (A.U.)
(080)
[010]
[100]
(350)
(550)
(040)
(330)
(530)
(220)
(310)
(200)
(400)
(800)
1
0
−1
q_y (Å^{-1})
q_x (Å^{-1})
0
2
4
6
b
2θ
220
Top view (intrinsic distortion)
a
b
c
400
Ordering
2θ′
Top view (reduced distortion)
a
b
c
c
Simulated
ΔI (A.U.)
[010]
[100]
(040)
(220)
(400)
q_x (Å^{-1})
q_x (Å^{-1})
d
(110)
(220)
(400)
(530)
(550)
(200)
(310)
(330)
ΔI (A.U.)
q_r (Å^{-1})
ΔI (1-3ps)
Debye-Waller
Simulated

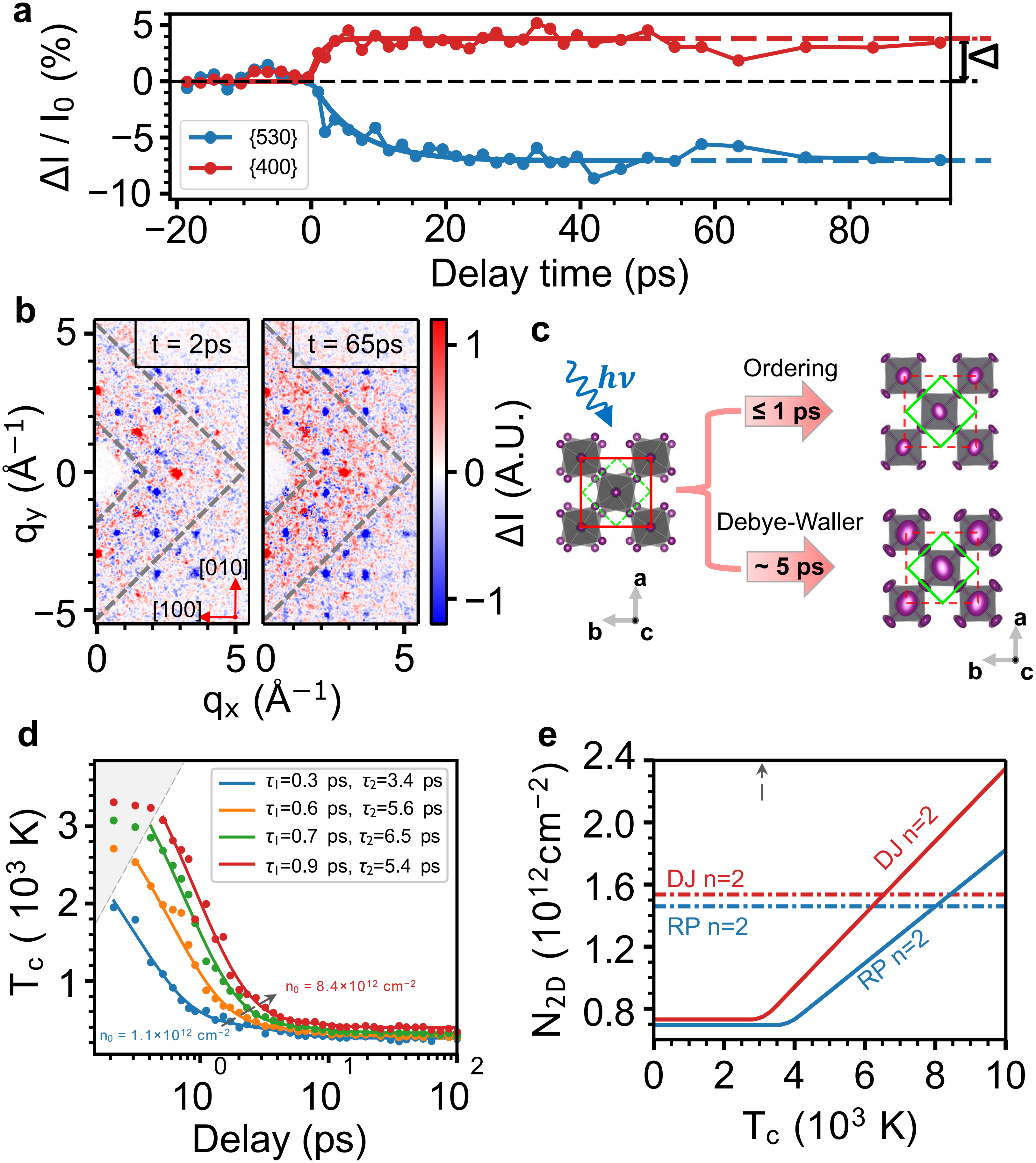
a
ΔI / I₀ (%)
5
0
−5
−10
−20
0
20
40
60
80
Delay time (ps)
{530}
{400}
Δ
b
t = 2ps
t = 65ps
[010]
[100]
qy (Å⁻¹)
qx (Å⁻¹)
5
0
−5
0
5
0
5
ΔI (A.U.)
1
0
−1
c
hν
Ordering
≤ 1 ps
Debye-Waller
~ 5 ps
a
b
c
a
b
c
d
Tc (10³ K)
3
2
1
Delay (ps)
10⁰
10¹
10²
τ₁=0.3 ps, τ₂=3.4 ps
τ₁=0.6 ps, τ₂=5.6 ps
τ₁=0.7 ps, τ₂=6.5 ps
τ₁=0.9 ps, τ₂=5.4 ps
n₀ = 8.4×10¹² cm⁻²
n₀ = 1.1×10¹² cm⁻²
e
N2D (10¹²cm⁻²)
2.4
2.0
1.6
1.2
0.8
0
2
4
6
8
10
Tc (10³ K)
DJ n=2
RP n=2
DJ n=2
RP n=2

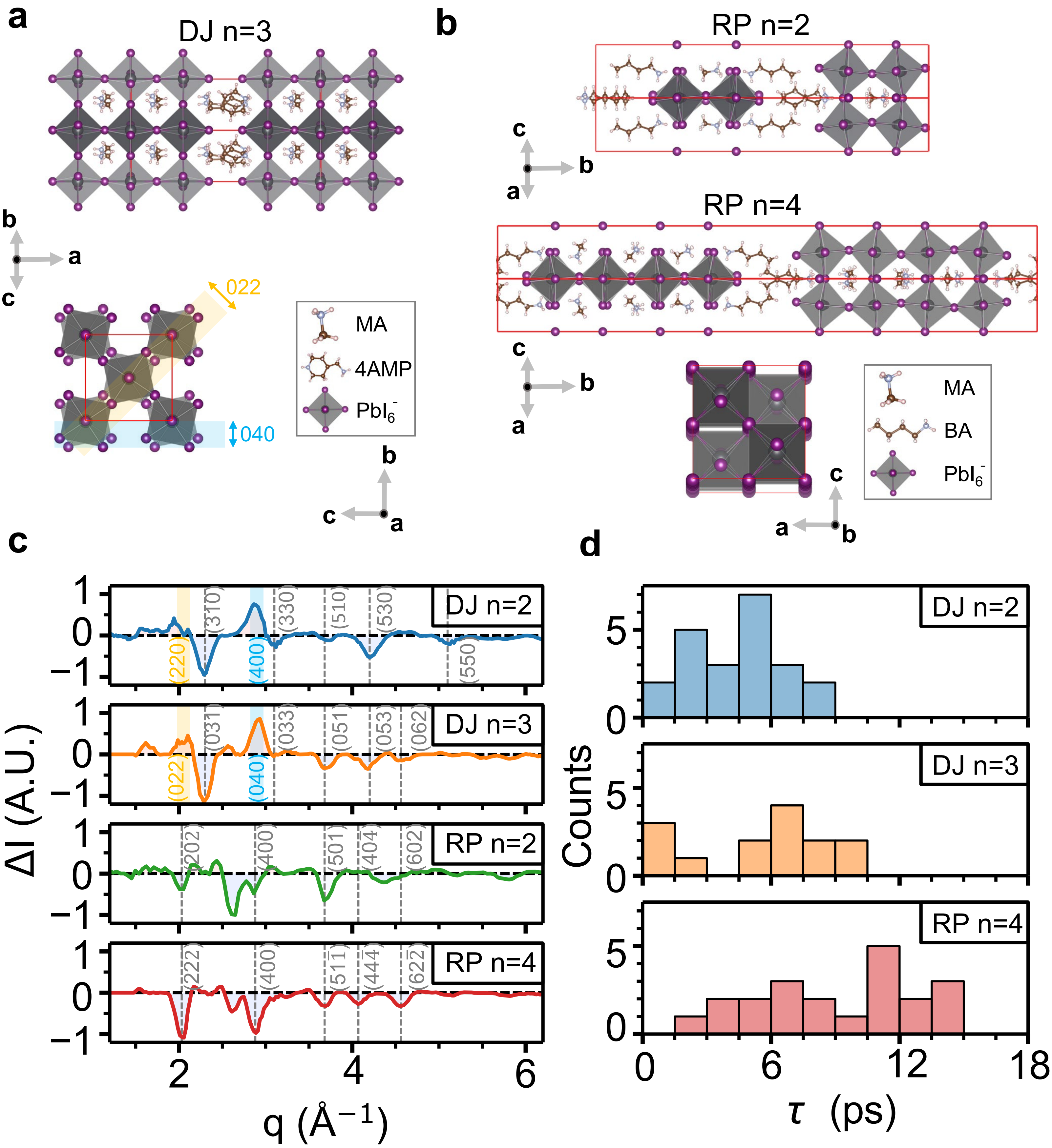
a
DJ n=3
b
a
c
022
040
MA
4AMP
PbI_6^-
b
c
a
b
RP n=2
c
b
a
RP n=4
c
b
a
MA
BA
PbI_6^-
c
a
b
c
ΔI (A.U.)
DJ n=2
(220)
(310)
(400)
(330)
(510)
(530)
(550)
DJ n=3
(022)
(031)
(040)
(033)
(051)
(053)
(062)
RP n=2
(202)
(400)
(501)
(404)
(602)
RP n=4
(222)
(400)
$(51\bar{1})$
$(44\bar{4})$
$(62\bar{2})$
1
0
−1
2
4
6
q (Å^{-1})
d
Counts
DJ n=2
DJ n=3
RP n=4
0
5
0
6
12
18
τ (ps)

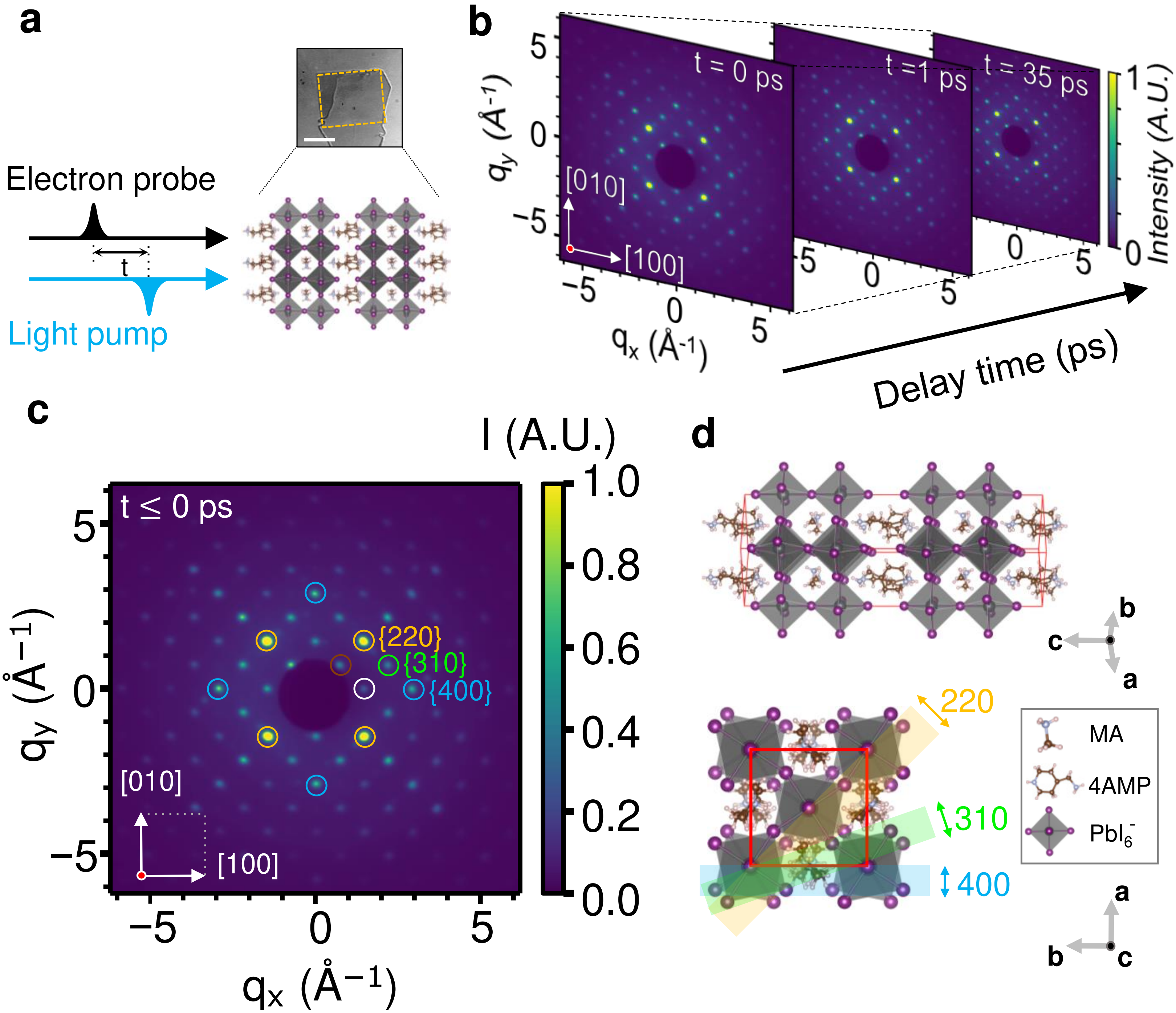
a
Electron probe
t
Light pump
b
t = 0 ps
t =1 ps
t = 35 ps
q_y (Å^{-1})
q_x (Å^{-1})
[010]
[100]
5
0
−5
Intensity (A.U.)
1
0
Delay time (ps)
c
t ≤ 0 ps
{220}
{310}
{400}
[010]
[100]
q_y (Å^{-1})
q_x (Å^{-1})
I (A.U.)
1.0
0.8
0.6
0.4
0.2
0.0
d
b
c
a
220
310
400
MA
4AMP
PbI_6^-
a
b
c

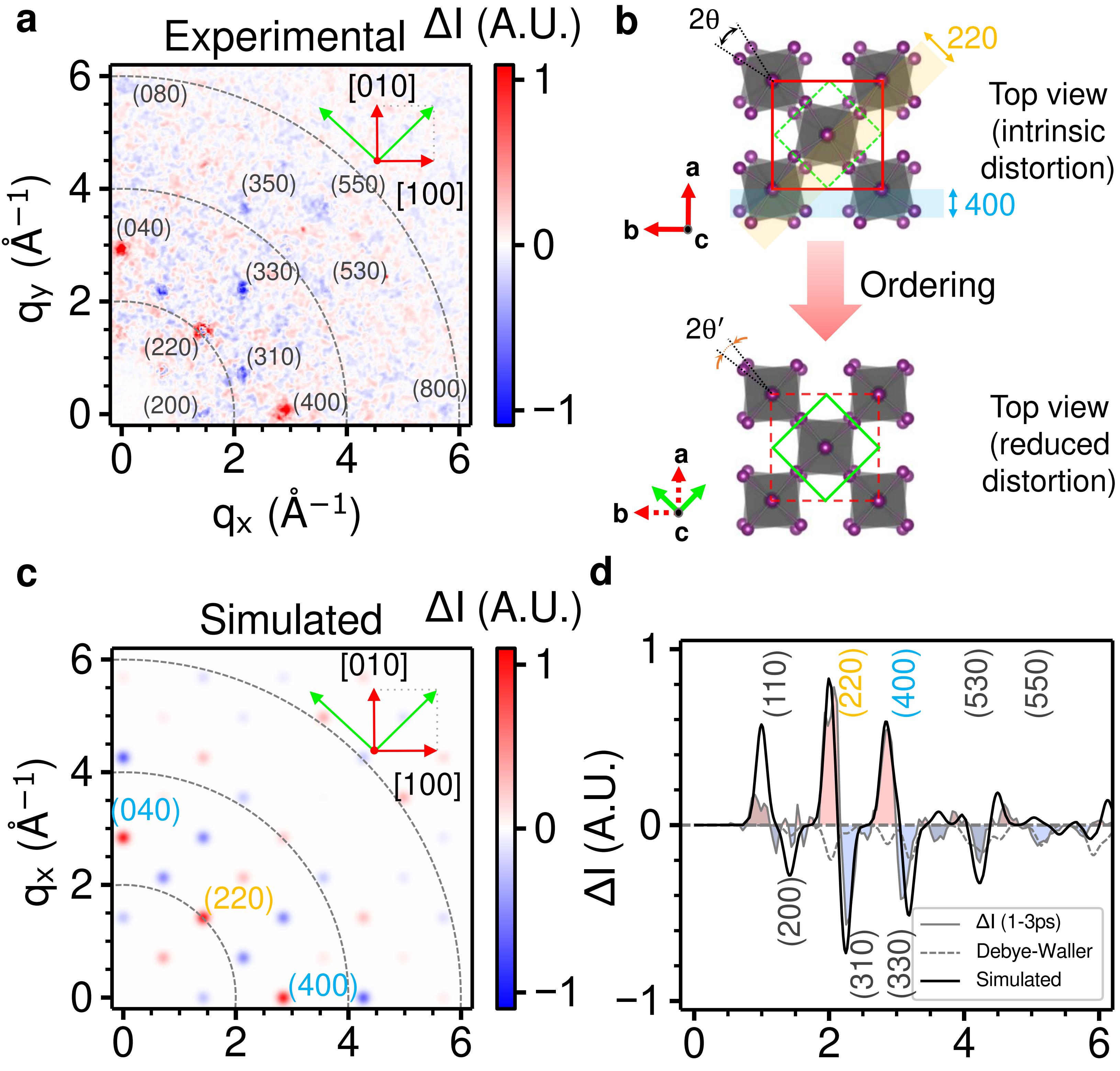
a
Experimental
ΔI (A.U.)
1
0
−1
q$_y$ (Å^{-1})
q$_x$ (Å^{-1})
0
2
4
6
[010]
[100]
(080)
(350)
(550)
(040)
(330)
(530)
(220)
(310)
(200)
(400)
(800)
b
2θ
220
Top view (intrinsic distortion)
a
b
c
400
Ordering
2θ′
Top view (reduced distortion)
a
b
c
c
Simulated
ΔI (A.U.)
1
0
−1
q$_x$ (Å^{-1})
q$_x$ (Å^{-1})
0
2
4
6
[010]
[100]
(040)
(220)
(400)
d
ΔI (A.U.)
q$_r$ (Å^{-1})
1
0
−1
0
2
4
6
(110)
(220)
(400)
(530)
(550)
(200)
(310)
(330)
ΔI (1-3ps)
Debye-Waller
Simulated

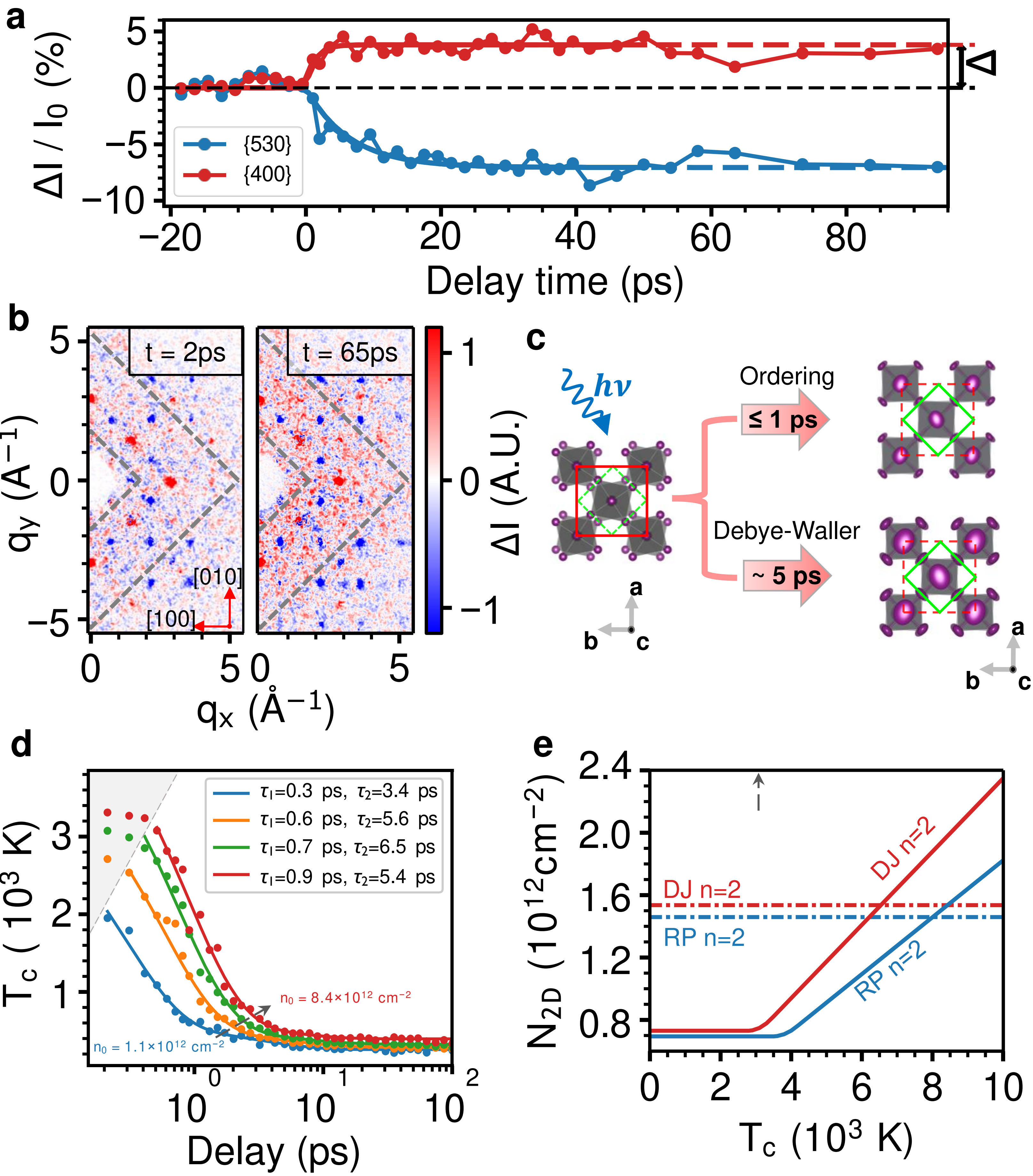

a
ΔI / I₀ (%)
5
0
−5
−10
−20
0
20
40
60
80
Delay time (ps)
{530}
{400}
Δ
b
t = 2ps
t = 65ps
q_y (Å⁻¹)
q_x (Å⁻¹)
[010]
[100]
ΔI (A.U.)
1
0
−1
5
0
−5
c
hν
Ordering
≤ 1 ps
Debye-Waller
~ 5 ps
a
b
c
d
τ₁=0.3 ps, τ₂=3.4 ps
τ₁=0.6 ps, τ₂=5.6 ps
τ₁=0.7 ps, τ₂=6.5 ps
τ₁=0.9 ps, τ₂=5.4 ps
n₀ = 8.4×10¹² cm⁻²
n₀ = 1.1×10¹² cm⁻²
T_c (10³ K)
1
2
3
10⁰
10¹
10²
Delay (ps)
e
N_2D (10¹²cm⁻²)
2.4
2.0
1.6
1.2
0.8
DJ n=2
RP n=2
DJ n=2
RP n=2
0
2
4
6
8
10
T_c (10³ K)

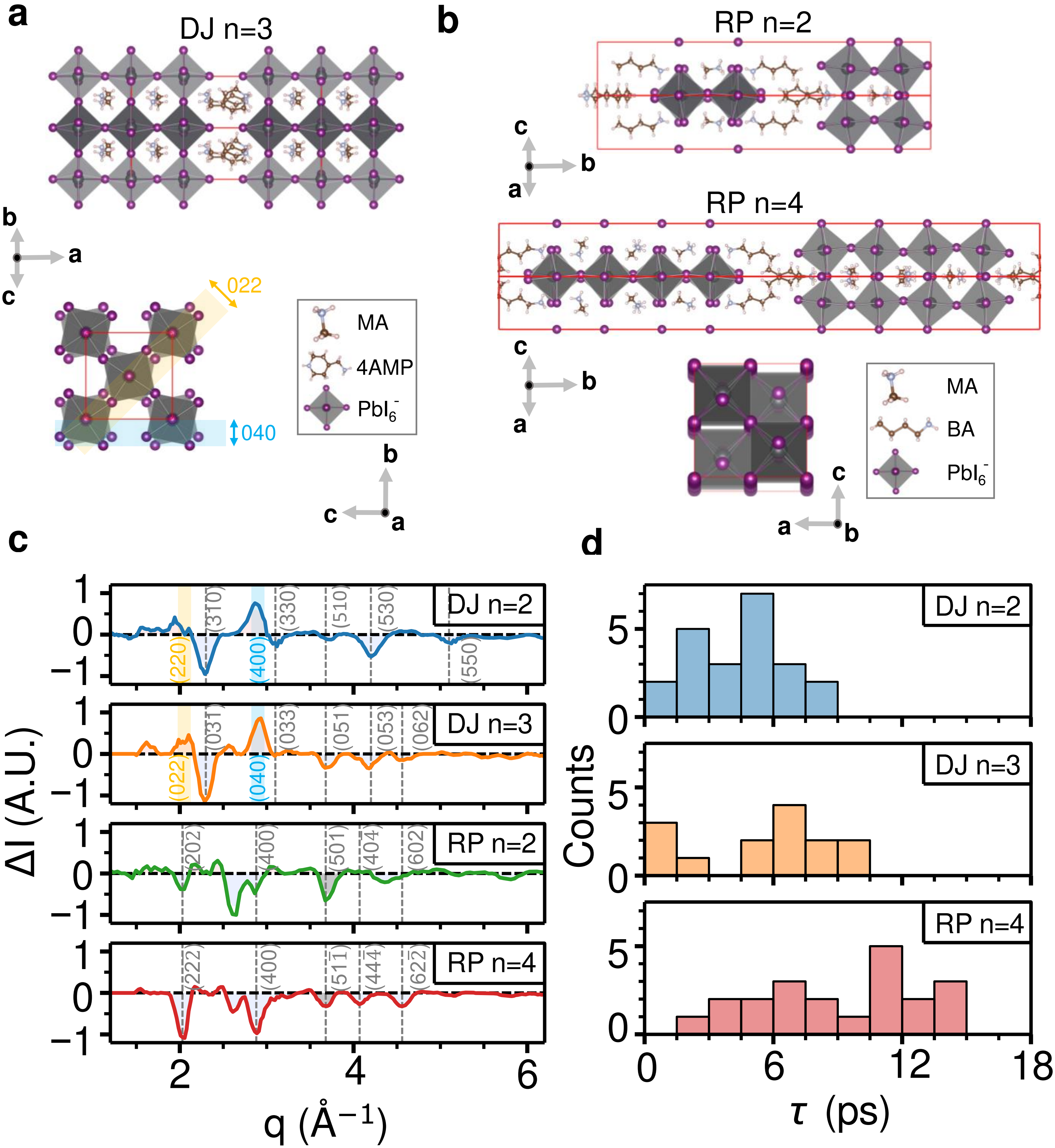
a
DJ n=3
b
a
c
022
040
MA
4AMP
PbI$_6^-$
b
c
a
b
RP n=2
RP n=4
MA
BA
PbI$_6^-$
c
DJ n=2
(220)
(310)
(400)
(330)
(510)
(530)
(550)
DJ n=3
(022)
(031)
(040)
(033)
(051)
(053)
(062)
RP n=2
(202)
(400)
(501)
(404)
(602)
RP n=4
(222)
(400)
(51$\bar{1}$)
(444)
(62$\bar{2}$)
ΔI (A.U.)
1
0
−1
2
4
6
q (Å^{-1})
d
DJ n=2
DJ n=3
RP n=4
Counts
5
0
0
6
12
18
τ (ps)

This PDF file includes:

Supplementary discussions 1-11
Figs. S1 to S26
Table S1 to S2
References

Table of Contents

Supplementary discussions 1 - 11

Supplementary discussion 1. Crystal orientation of DJ n=2, DJ n=3, RP n=2 and RP n=4 crystals

The crystal orientation of each sample measured in UED was acquired by comparing the diffraction patterns with the simulated diffractions viewing at different directions.

For the DJ systems, the experimental patterns in Fig. S2b (DJ n=2) and Fig. S13b (DJ n=3) show great consistency with the simulated ones (Fig. S2a & Fig. S13a) viewed at stacking axis direction ([001] for DJ n=2, and [100] for DJ n=3), confirming the horizontal orientation of the DJ crystals, where the perovskite crystal layers are parallel to the substrate. The azimuthally integrated plots (Fig. S2c for DJ n=2, Fig. S13c for DJ n=3) also show good agreement in peak locations and convoluted intensities. The measured in-plane Bragg peaks can be properly indexed accordingly, including (hk0) for DJ n=2, and (0hk) for DJ n=3. The labeled peaks are shown in 2D patterns and azimuthally integrated plot.

For RP n=2 crystal, the simulated pattern along stacking axis [010] is shown in Fig. S20a, where all the peak locations agree with the experimental ones in Fig. S20b, confirming the major orientation of the RP n=2 crystal is horizontal, same as DJ crystals discussed above. Additionally, concentric rings are observed between q=2 $Å^{-1}$ and 3 $Å^{-1}$, as observed in Fig. S20b, suggesting the existence of poly-crystalline like crystal structure with mixed orientations. The azimuthally integrated plots (Fig. S20c) show good agreement in peak locations and convoluted intensities, with additional unassigned peaks at q=2.6 $Å^{-1}$ and 3.7 $Å^{-1}$. We've excluded the possibility of PbI_2 diffraction by comparing with the electron diffraction of PbI_2 thin film.[1] We attribute them to the possible perovskite diffraction from out-of-plane or mixed directions, or an unidentified phase of 2D perovskites, and have excluded them from the discussion of in-plane Bragg peaks responses of RP n=2 crystals.

For the RP n=4 crystal, the simulated pattern along stacking axis [010] is shown in Fig. S21e, with corresponding 1D azimuthally integrated plot in Fig. S21f. However, this pattern doesn't match with the experimental one (Fig. S21a) based on the following observations: 1) more peaks are observed in static UED patterns, such as q=2.2$Å^{-1}$ and 3.8 $Å^{-1}$ as shown in Fig. S21f; 2) anisotropic intensity distribution along q_x and q_y directions, which is different with Fig. S21e with 4th fold symmetry. Therefore, we conclude the beam direction is not perfectly along the stacking axis as observed in DJ and RP n=2 crystals. As shown in Fig. S21c & Fig. S21d, we find that the [011] orientation gives the best match for RP n=4, with 7.8 degrees deviation from stacking axis [010], as sketched in Fig. S21b. As a result, some out-of-plane Bragg peaks can be detected as well, which may explain the anisotropic UED response between q_x and q_y directions, including the intensity change shown in Fig. S15 and the time constants shown in Fig. S16.

Supplementary discussion 2. Sample Thickness and Carrier Density Estimation

Crystal thickness determination: The thickness of the crystal was determined by comparing the absorbance spectrum with the estimated one calculated from absorption coefficient of 2D perovskites. Here we have referenced the absorption coefficients obtained from ellipsometry by Song et al.[2] Applying Beer-Lambert's law and neglecting light scattering, the relation of crystal thickness d and crystal transmission (T) is given by:

$$T = \frac{I}{I_0} = 10^{-OD} = e^{-\alpha d} \tag{S2.1}$$

Where OD is the absorbance in optical density determined by transmission (I/I_0), and α is absorption coefficient. The comparison of experiment and simulated absorbance spectrum is depicted in Fig. S1.

Carrier density: The light-injected carrier density in quantum well is estimated by:

$$n_0 = \frac{\Phi/(hv)\, A}{d/l_w} \tag{S2.2}$$

Where Φ stands for energy fluence of each pulse (mJ/cm^2), hv stands for excitation phonon energy (3.1 eV for UED), A stands for absorbance of the sample, d is the sample thickness, and l_w is the width of quantum-well in 2D perovskites.[3,4] Here, we've neglected the sample reflection and estimated the sample absorbance by transmission data in Fig. S1. As a result, the list of thickness and corresponding carrier densities of each measurement is shown in Table S1.

Supplementary discussion 3. Time constants of Bragg peaks of DJ and RP crystals.

A. *DJ perovskites*

Time traces of the Bragg peak families of DJ n=2 are shown in Fig. S3, with rapid rise (τ~1ps) in {400}, as well as slower decay (scale of 5ps) of the other major group families. List of fitted intensity change (Δ (%)) and time constant (τ) of each Bragg peak (hk0) is listed in Fig. S7. Both the intensity changes and time constants show a significant anisotropy with respect to directions in the DJ n=2 crystals, which reflects the lack of a tetragonal axis in the monoclinic centered structure (space group Cc n°9) of the crystals at rest because of the geometry and structure of the 4AMP cation. We also note that the intensity traces of some Bragg peaks such as {330} and {550} show a long recovery time (τ>30 ps, Fig. S3a), which could be related to other heat transfer mechanisms and phonon-phonon interactions.[5]

The responses of time scales are similarly observed in DJ n=3, including a fast rise in {040} (Fig. S13), and similar distribution of time constants for other Bragg peak families (Fig. 4d, corresponding scatter plot shown in Fig. S18).

B. RP perovskites

As suggested in Fig. 4d, comparison of the histograms of the time constants τ for DJ n=2, DJ n=3, and RP n=4 shows a generally slower response (up to 15 ps) for RP perovskites as compared to the DJ crystals. Besides, different dynamics are observed for (400) peaks in RP (Fig. S13).

The slow response time in RP systems can arise from the differences in the lattice softness between the BA and the DJ 2D perovskites. The BA molecules reduce the rigidity of the 2D lattice by comparison to the DJ case, leading to an enhancement of the lower-energy part of the vibrational density of states.[6] It was indeed shown experimentally to enhance the deformation potential mechanism in BA compounds, leading to carrier trapping.[7] This results is also consistent with a recent study on high-resolution resonant impulsive stimulated Raman spectroscopy,[8] showing that the vibrational relaxation in monolayered bromide perovskites relatively fast with flexible alkyl-amines.

Supplementary discussion 4. Possible reasons of Bragg peak increase in DJ perovskites.

In this section, we discuss several possible mechanisms that can cause an increase in the Bragg peaks, such as phase transition,[9] and multiple scattering in monocrystalline samples.[10] No signature of phase transition is found in DJ n=2 perovskites, and we exclude possible effect of by the estimation of extinction distance under MeV electron beams, which is much larger than the sample thickness.

A. *Phase transition from thermal lattice heating.* One of the possible mechanisms that induces the collective lattice ordering in DJ perovskites is the thermally induced phase transition from local lattice heating. To investigate the thermal response of DJ n=2 crystals, we first estimate the temperature jump induced by the laser pump, then using the differential scanning calorimetry (DSC) and temperature dependent XRD results to exclude the possible phase transition effect.

a. *Estimation of temperature jump.*

The local lattice temperature increase is estimated by total input pump energy and samples' specific heat. For DJ n=2 crystals, a carrier density of 2.5×10^{13} cm^{-2} corresponds to a bulk carrier concentration of $n=1.4\times10^{20}$ cm^{-3}, which induces total energy into the lattice:

$$\Delta E = n \times \left(E_{pump} - E_g\right) = 1.4 \times 10^{20} \times (3.1 - 2.2)\ eVcm^{-3} = 20.16\, J/cm^3 \tag{S4.1}$$

The mole of the DJ n=2 crystal is calculated from crystal structure (4 molecules per unit cell):

$$m = \frac{1}{V_{UC}} \times \frac{4}{N_A} = 2.53 \times 10^{-3} mol/cm^3 \tag{S4.2}$$

The specific heat of DJ n=2 at T~300K is estimated from DSC measurement, as shown in Fig. S9:

$$C_p = 0.54\, J\, K^{-1} g^{-1} = 728\, J\, K^{-1} mol^{-1} \tag{S4.3}$$

And the corresponding estimated temperature jump is:

$$\Delta T = \frac{\Delta E}{m * C_p} \sim 11K \quad \text{(S4.4)}$$

b. *Differential scanning calorimetry (DSC) results*.

To investigate possible thermal phase transition induced by lattice heating, differential scanning calorimetry (DSC) was performed from room temperature to 150℃, as suggested in Fig. S9. From the DSC curve, no significant phase transition is observed. Based on over estimation of temperature increase induced by light (SI discussion 6), the local temperature increase in the crystal lattice is below the 15K and no possible phase transition is observed or reported in this range.[11] Therefore, we conclude the collective lattice ordering in light-induced in ultrafast scale, instead of thermally induced caused by lattice heating.

c. Temperature dependent XRD.

Additionally, we performed temperature XRD from room temperature to 55°C, data shown in Fig. S10. As we can see, most of the Bragg peak intensities go through a slight decrease with increasing temperature due to the presence of Debye Waller effect.

Here we focus on the in-plane Bragg peaks, primarily related to the edges and diagonal of the perovskite octahedral, which is our main focus in-plane diffraction patterns in DJ n=2. Fig. S10 (b)(c)(d) plot the peak profile variation with respect to the sample at room temperature, zoomed at q- regions near (220) and (400) respectively. As we can see, both (220) and (400) peaks exhibit slight intensity decrease, which is contradictory with the UED response.

Besides the intensity variations from observed from temperature XRD, we also observed a global peak shifting (upto 0.15%, Fig. S10 (f)). A global shifting of Bragg peaks toward low-q values is generally expected from the thermal expansion. However, this behavior of Bragg peaks shifting is not resolved in the UED. We attribute the absence of thermal expansion signature in UED diffraction patterns to the low q resolution of the UED measurements (≈0.17Å^{-1}).

In fact, the transient increase in the collective ordering in the DJ n=2 lattice may be viewed as an ‘incomplete transformation’ towards a completely ordered phase. Indeed, no evidence of phase transition is found from differential calorimetry and XRD. Additionally, the perfectly undistorted 2D perovskite reference phase has only been observed in the fully inorganic Cs-based Cs2PbI2Cl2 2D perovskite at room temperature,[12] which emphasize the importance of the anisotropy of the 4AMP organic cations in the structure for the lattice distortion in hybrid 2D perovskites. On the contrary, undistorted phases are common for hybrid 3D perovskite compounds at room temperature and therefore any ultrafast light-induced ordering is lacking.[13]

B. *Multiple scattering effect.* Another possible mechanism would be the possible multiple scattering effect in single-crystalline samples, as reported by Vallejo et al using keV electron beams.[10]. In fact, as pointed out by Vallejo et al, the possibility of having multiple scattering will rely on a characteristic length known as the extinction distance ($\xi_{\mathbf{g}}$) of the samples, which is strongly affected by the electron beam energy, crystal structure and elements of material (Williams & Carter 2008[14]) as described by the following formula,

$$\xi_{\boldsymbol{g}} = \frac{\pi V cos\theta_B}{\lambda F_{\boldsymbol{g}}} \tag{S4.5}$$

Where V is the volume of the unit cell, θ_B is Bragg angle, λ is electron wavelength, and F_g is the structure factor at diffraction vector $\boldsymbol{g}$.

The calculation of V, λ, and θ_B is straightforward. For high energy electrons θ_B is fairly close to 0, since the electron wavelength λ is much smaller than lattice spacing (θ_B=0.5 deg for Si (220) at 100keV) and therefore $\cos\theta_B \approx 1$. The F_g is estimated by the summation of all the atomic scattering factors with different atomic locations within the unit cell (Williams & Carter 2008 [14], Page 223):

$$F_g = F_{hkl} = \sum_{i=1}^{n} f_i^{(e)}\, e^{-2\pi i(hx_i + ky_i + lz_i)} \tag{S4.6}$$

The atomic scattering factor is a function of scattering vector s ($s = \sin\theta/\lambda$). and a common approximation is fitted with the following formula[15]:

$$f^{(e)}(s) = \sum_j a_j \exp(-b_j s^2) \tag{S4.7}$$

The coefficients of a_j, b_j for each atoms are listed in Table 1 in Peng et al[15]. For ionized atoms (such as Pb2+ and I-), additional term is included[16].

Based on the information above, we have estimated the extinction distance for Si under 100keV and DJ n=2 perovskites under 3.7MeV, which are given by:

$$\begin{aligned} \xi_{\boldsymbol{Si}|(\mathbf{220})} &= \frac{\pi V cos\theta_B}{\lambda F_{\boldsymbol{g}}} = \frac{\pi *\ 163.6\text{Å}^3 * 1}{3.70e - 2\text{Å} *\ 15.06\ \text{Å}} = 92\ nm \\ \xi_{\boldsymbol{DJ}\mathbf{2}|(\mathbf{220})} &= \frac{\pi V cos\theta_B}{\lambda F_{\boldsymbol{g}}} = \frac{\pi * 2627\text{Å}^3 * 1}{2.97e - 3\text{Å} *\ 261.73\ \text{Å}} = 1062\ nm \end{aligned} \tag{S4.8}$$

The calculation of Si is close to the value reported in the literature (75.7 nm)[14], giving a fair estimation. Compared to the sample thickness of d≈270nm of DJ n=2 crystal, the extinction distance is ~4 times larger, therefore we believe the multiple scattering effects are not likely to happen in DJ n=2 perovskites.

Furthermore, in order to give a clear demonstration of the absence of multiple scattering, we have simulated the diffraction pattern of DJ n=2 based on kinematic scattering theory following the assumptions of weak-phase object approximation, which is a commonly used to model the crystal diffraction from electron microscopy.[17,18] The calculated pattern for 4 by 4 supercell is shown in Fig. S22. The simulated diffraction in Fig. S22(b) gives a reasonable match to the experimental diffraction of the crystal at rest Fig. S22(a), and are also in consistency with the calculations in Fig. S2(a), which is directly evaluated from the structural factor: $I_{hkl} \propto |F_{hkl}|^2$. Furthermore, the absence of Kikuchi lines in the scattering pattern also suggests lack of multiple scattering (FIG. S22(c)).[19] A quantitive comparison of the linecut of the patterns is also displayed in FIG. S22(d), which gives a reasonable agreement for the intensity distribution of the Bragg peaks, especially at (400), (310) and (220) which shows the most contrast in the differential response (Fig. 2d) and are the most relevant peaks in the discussion of lattice ordering. This consistency indicates the kinematical scattering will be sufficient to describe the diffraction patterns, and the multiple scatterings are negligible.

Supplementary discussion 5. Estimation of antiferro-distortion in 2D perovskites

A. *Simplified model involving rigid octahedral rotations.*

Fig. S5 shows the simulated diffractions with intrinsic (Fig. S5a) and reduced antiferro-distortion (Fig. S5b), as well as the corresponding crystal structures with different disordering parameter viewed along stacking axis. The top (in-plane) view of 2D perovskite caused by intrinsic in-plane cell doubling is shown in the schematics in Fig. S5c. The tilted angle between adjacent octahedra (2θ = 24°) is associated with antiferro-distortion, forming an initially doubled unit cell of 8.8 Å (indicated in red squares), as opposed to the undistorted structure (θ = 0°) where unit cell is of 6.2 Å (labeled by green squares). To estimate the influence on crystal structure with reduced antiferro-distortion, we've constructed a hypothetic structural phase (Fig. S5d), where interlayer octahedra are more aligned and simulated an electron diffraction pattern correspondingly (Fig. S5b). For a direct comparison between the symmetrized and the intrinsic antiferro-distorsive phase, a subtracted diffraction pattern is displayed in Fig. 2c. As we can see, the intensity variations are expected in specific Bragg planes, including {400} and {220} (bright red) increasing and {310} and {530} (blue).

To estimate the light-induced rotation angle $\Delta\theta = \theta' - \theta_0$, we calculated the percentage of Bragg peak intensity variation as a function of tilting angle (Fig. S5e), and compare them with the experiment data at early time (t = 2ps). From the responses of {310}{400}, we estimated the optimal order parameter to be θ =11.75°, as shown in the shadow region in Fig. S5e, corresponding to an octahedral tilt of $\Delta\theta$ = 0.25°.

B. *Phonon mode simulations on DJ n=2 crystals.*

Besides the simplified model involving pure rigid tilting of octahedra, we believe a more complex model should involve a shift of crystal structure along the eigenvectors of specific normal modes. Therefore, we perform DFT computations on DJ n=2 (Phonon Simulation methods) and suggest several possible vibrational modes candidates, as well as the related diffraction plots, which are listed in Fig. S6. These normal modes are indeed related to the antiferro-distortions (Fig. S6a, c, &e), and shifting the crystal structure along these eigenvectors result in a positive change along {220} and {400} directions, consistent with the prediction in section A. Therefore, these calculations further confirmed our hypothesis on lattice ordering (Fig. 2).

Supplementary discussion 6. Transient absorption spectroscopy of DJ n=2 crystal and carrier temperature extraction.

The transient absorption (TA) measurements are performed on nearly identical 2D perovskite crystals (similar lateral size L≈200um, thickness d≈300nm and composition (DJ n=2) as used for UED). We used an optical pump set at 3.1 eV (same as UED) with 0.1-0.75 mJ/cm^2 (1.1×10^{12} cm^{-2} - 8.4×10^{12} cm^{-2}, corresponding to an excitation regime similar than in the UED measurements), followed by a white-light probe monitoring the transmission variations of the sample (see Method Section on transient absorption spectroscopy). Therefore, for similar optical pump conditions, we had access to an optical probe in TA, yielding complementary information with respect to the structural ones provided by the UED experiment. The results are displayed below in Fig. S11.

From our TA data, several major observations are summarized:

A. Strong bleaching of exciton states. Fig. S11 (c) shows absorbance spectra at different fluences. We observed a significant bleaching of the exciton peak at 2.18eV monotonically increasing with excitation densities upto 0.75 mJ/cm^2. From our TA studies extrapolated to a fluence of 1-2 mJ/cm^2, we will expect an almost complete bleaching of the exciton resonance leading essentially to a hot electron-hole pair plasma just after the pump in the UED experiment. Furthermore, Fig. S11(f) shows a long lifetime ($\tau \sim 10^2$ps) of exciton dynamics, indicating a high density of carriers is still bleaching the exciton resonance over long time, consistent with the observed long lifetime of lattice response in UED.

B. Hot-carrier cooling dynamics. As indicated in Fig. S11 (b), at 0.75 mJ/cm^2, we have observed the cooling phenomenon starting at t~0.4 ps, which is consistent with the typical values reported in halide perovskites.[20,21] We estimated the evolution of the effective carrier temperature after t~0.5ps by fitting the high-energy tail near the band edge with a Maxwell-Boltzmann distribution (Fig. S11 (b)), which is a commonly used method to approximate the carrier temperature in semiconductors.[22] As estimated in Fig. 3(c), the first cooling process of hot-carriers ranges from sub-ps to 1 ps. The initial carrier temperature is fitted to be T_c≈3700K for 0.75 mJ/cm^2. We extrapolate this value to be 3300K for a fluence of 1 mJ/cm^2 in the UED experiment.

C. Long-lived coherent acoustic waves. As shown in Fig. S12, we observed a low-frequency oscillations from TA data, which is related to coherent acoustic waves. Through Fourier transform in frequency domain, (Fig. S12(b)), we identify one phonon mode at 0.022 THz (0.09meV), related to temporal period of 45 ps, and are consistently observed for all the measured fluences (0.1-0.75mJ/cm^2). The activation of coherent acoustic modes with >100 ps lifetime suggest a long equilibration time of the phonon bath, on a time scale consistent with the long lifetime of the lattice response in UED.

These TA results suggest that hot electron-hole plasma may be more dominant at this high excitation densities, where many-body interactions and other non-linear processes could play a crucial role, contradictory to the work of Thouin et al. where the excitonic regime is mainly discussed.[23] This conclusion is also confirmed by the quantitate analysis defining the excitation regime and carrier saturation densities vs temperature which are shown below in discussion 7.

In addition to

Supplementary discussion 7. Estimation of saturation densities in DJ n=2 and RP n=2 crystals

We've estimated the carrier temperature in 2D perovskites to be T_c~3300K for 1mJ/cm^2. (Discussion 6). The next step consists in computing the saturation densities for the excitonic resonances in the DJ n=2 compound. For that purpose, the binding energy and the Bohr radius of the 1S exciton resonance are considered.[24] It is usually considered that the binding energy is reduced in DJ compounds by comparison to RP ones for the same n, but precise experimental data are not available for DJ n=2. We started from the known values available for RP n=2:[25] $E_{,b,RP}$=245meV for the binding energy and $a_{B,RP}$=1.60 nm for the effective Bohr radius related to the diamagnetic shift. Next, the effect of the smaller interlayer spacing is estimated using the effective dielectric model of Ishihara et al[26] $\varepsilon_{\text{eff,RP}}$=4.9 vs $\varepsilon_{\text{eff,DJ}}$=5.5, leading in turn to a reduction of the binding energy $E_{b,DJ}$=204meV. The BSE model[25] was then used to compute the diamagnetic shift and finally a $_{B,RP}$=1.56 nm. A summary of saturation densities at different carrier temperate is plotted in Fig. 3e.

Supplementary discussion 8. Generalizability of lattice response and order parameter on 3D perovskites.

In this section, we compare the distinct ultrafast lattice dynamics of different perovskite systems, and discuss the generalizability of other parameter in 3D perovskites. We believe the initial antiferrodistorsive states are indeed important, not only for 2D perovskites but also for the 3D perovskites. The antiferro-distorsive octahedral rotation angles of both 2D and 3D perovskites systems are listed in table S2.

A. 3D iodine perovskites ($MAPbI_3$)

Wu et al have performed the same UED measurements on the polycrystalline thin film of $MAPbI_3$.[1] The behavior of the Bragg peaks is Debye-Waller like, and no similar response involving reduction of antiferro-distortion has been observed. Here, in order to examine the generalizability of the order parameter in 3D perovskites, we have performed a similar simulation with a hypothetic octahedral rotation model (similar as the one described in the manuscript Fig.2), and compare the expected variations of diffraction intensities to the experimental curve from Wu et al. The comparison is shown in Fig. S23.

As shown in Fig. S23, the reduction of the antiferro-distorsion present in the tetragonal phase of $MAPbI_3$, should lead to positive intensity variations at q=2.0 and 2.8Å-1, similar to the ones observed for DJ n=2 (Fig. 2d) as a result of reduced in-plane octahedral rotation towards higher symmetry phase. Indeed, the characteristic positions of the Bragg peaks related to the perovskite backbone are similar in iodide-based 2D and 3D perovskites, because these compounds share similar lengths for the Pb-I bonds. However, by comparing the simulated differential pattern with the UED results for $MAPbI_3$ from Wu et al, such positive response is not observed in the experimental scattering intensity at different delay times (t=5, 70ps), as indicated in Fig. S23(a). In fact, we note that MAPbI3 exhibits a similar behavior than RP phases (Fig. 4, also zoomed in at same q region in Fig. S23(b)), especially in RP n=4 which is close to 3D perovskites. We believe that the consistency of negative intensity response in both 2D RP perovskites and 3D perovskites provide clear evidence of the distinct lattice dynamics in 2D DJ perovskites. The initial distortion generated by the presence of di-cations in DJ perovskites instead of mono-cations for RP perovskites is important, leading to different space groups, interlayer shifts and in-plane octahedra tilts (Mao et al[3]). From that perspective, the perovskite backbone in RP phases is less influenced by the flexible BA cations in the barrier and exhibit tilt patterns similar to bulk $MAPbI_3$.

B. *Oxide perovskites ($SrTiO_3$ & $KTaO_3$)*

For oxide perovskite systems, pristine $SrTiO_3$ presents a cubic structure at room temperature and goes through an antiferro-distorsive phase below Tc (105K). The phase transition is antiferro-distorsive with an order parameter related to an octahedral rotation ($\phi \sim 2°$ for T = 5K[27]) and a Bragg superlattice reflection. Indeed, Porer et al observed an ultrafast relaxation of antiferro-distorsive phase in Ca: $SrTiO_3$, where alloying with Ca was used to increase Tc (280K) and initial rotation angle. As observed by Porer et al, this ultrafast lattice dynamics, characterized by superlattice diffraction, is consistently observed in the tetragonal phase below the critical temperature, where a non-zero rotation angle is present at equilibrium. This suggests that similar to our work, an initial octahedral tilt is necessary to give rise to the ultrafast dynamics involving relaxation of antiferro-distortion phase.

In general, in oxide perovskites, distortions can be grouped into two categories:[28,29] either antiferro-distortions (e.g. $CaTiO_3$, $SrTiO_3$) related to the octahedral tilt, or ferroelectric distortions (e.g. $BaTiO_3$), where the B-site atom is displaced within surrounding octahedron. The observation of two types of distortions can be explained by the Goldschmidt tolerance factor.[28] In the case of $KTaO_3$, the ferroelectric order parameter, is connected to the off centering of B-site cation.[30] Therefore, we believe that our results on DJ 2D perovskites rather share some similarities with the reduction of antiferro-octahedral rotation in $SrTiO_3$ with photodoping as reported by Porer et al.

Supplementary discussion 9. Comparison of electron-LO phonon coupling with RP and DJ n=3.

To elucidate the strength and coefficients of the electron-LO phonon interactions, we performed temperature-dependent PL on DJ n=3 perovskites, where we monitor the linewidth of PL broadening as a function of temperature. The result is shown in Fig. S24.

The PL of DJ perovskite shows an asymmetric shape with two profiles. Here we focus at the dominant exciton emission at higher energy and plot the FWHM as function of temperature (Fig. S24(b), blue). Such behavior is also compared with RP n=3 (displayed in orange).

Here, the linewidth of DJ perovskites shows an anomalous broadening below 80K, which is similarly resolved in $MAPbI_3$ system[31], and is most likely also related to the influence of a phase transition in this temperature range. However, far above 80K in a temperature range relevant for the discussion of the present work, the broadening in DJ perovskites is consistent with the one in RP perovskites. It suggests that the strengths of the electron-phonon coupling in DJ n=3 and RP n=3 perovskites are not significantly different at high temperatures, and that the observed lattice ordering in DJ perovskites is not due to a specific electron-LO phonon coupling, which would otherwise cause similar lattice response between RP and DJ perovskites.

<u>**Supplementary discussion 10.** Estimation of long-time Bragg peak response and light-induced atom RMS displacements $\langle u^2 \rangle$</u>

Due to the deviation of Debye-Waller response (Fig. S25) of DJ n=2 crystal, the Bragg peaks intensity responses show competing effects between the conventional Debye-Waller effect and incipient anisotropic lattice ordering:

$$I_{total}(\vec{q}) = [I_0(\vec{q}) + \Delta I(\vec{q}, \Delta\theta)]\, e^{-\frac{1}{3}\Delta\langle u^2 \rangle\, q^2} \tag{S7.1}$$

Here $I_0(\vec{q})$ stands for the diffraction intensities at rest. The total Bragg peak intensity response have two contributions: i) an initial ordering process represented in $\Delta I(\vec{q}, \Delta\theta)$, where $\Delta\theta$ is the change of distortion angle (shown in Fig. 2b), which is estimated in Supplementary discussion 5. $\Delta I(\vec{q}, \Delta\theta)$ is simulated based on reduction of andiferro-distortion and also shown in Fig. 2c. ii) classical thermal energy transfer involving all the Bragg peaks, represented in Debye-Waller effect as exponential term $e^{-\frac{1}{3}\Delta\langle u^2 \rangle\, q^2}$, where $\langle u^2 \rangle$ stands for atomic mean squared (RMS) displacement.

The competing effect of the two mechanisms is also indicated in Fig. S8, where considering only the first contribution (gray dashed line, Fig. S8(b)) will not give a good prediction at long delay time (40-80 ps) especially at higher q, while the combining effect of the two (black solid line) matches better with the experimental response. By comparing the simulated intensity change with the Bragg peak response at long time, the Debye-Waller factor is estimated to be 1.6×10^{-3} Å^{-2}, corresponding to light-induced atom RMS displacement of $\sqrt{\Delta\langle u^2\rangle} \sim 0.07$ Å at carrier density of 2.5×10^{13} cm^{-2}.

Supplementary discussion 11. Time evolution of diffraction intensities through the UED run.

Fig. S19 shows the time evolution over ~2 hours during the UED run of DJ n=2 crystal. As shown in Fig. S19a, the total diffraction intensity doesn't show a significant drop over ~2 hours, suggesting the crystal structure remains stable throughout the experiment. Fig. S19b shows the comparison of the electron diffractions between 0min and 120mins, where all the Bragg peaks remain existing, with a slight decrease of overall intensities. Additionally, no rings or new peaks were formed through the experiments (Fig. S19c and Fig. S19d), confirming that no evidence of possible sample degradation or damage is found.

Supplementary Figures S1 – S26

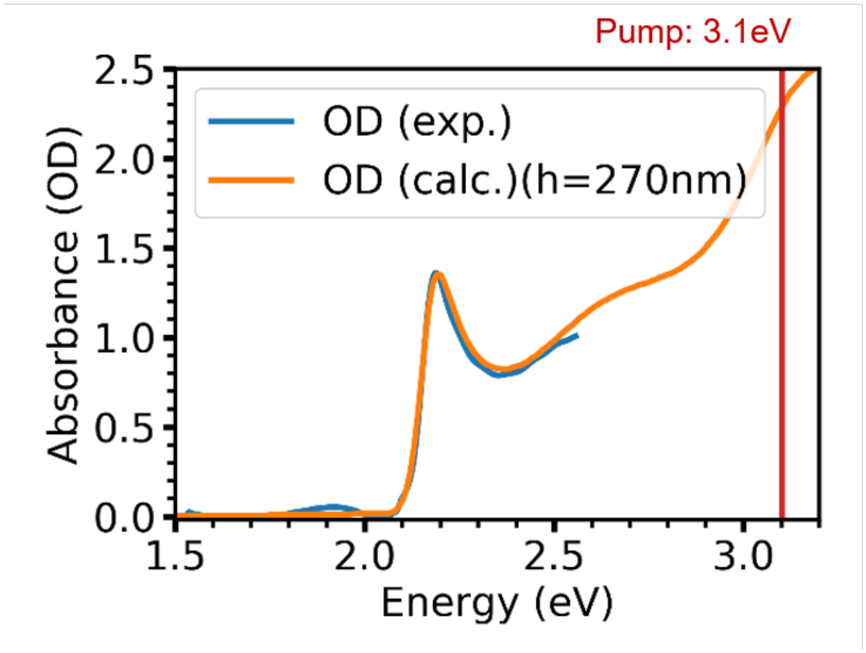

Fig. S1 | Optical absorbance spectra of DJ n=2 crystal. The measured absorbance is shown in blue line, with calculated absorbance (orange line) with crystal thickness of 270nm, estimated from the absorption coefficient as reported by Song et al.[3]

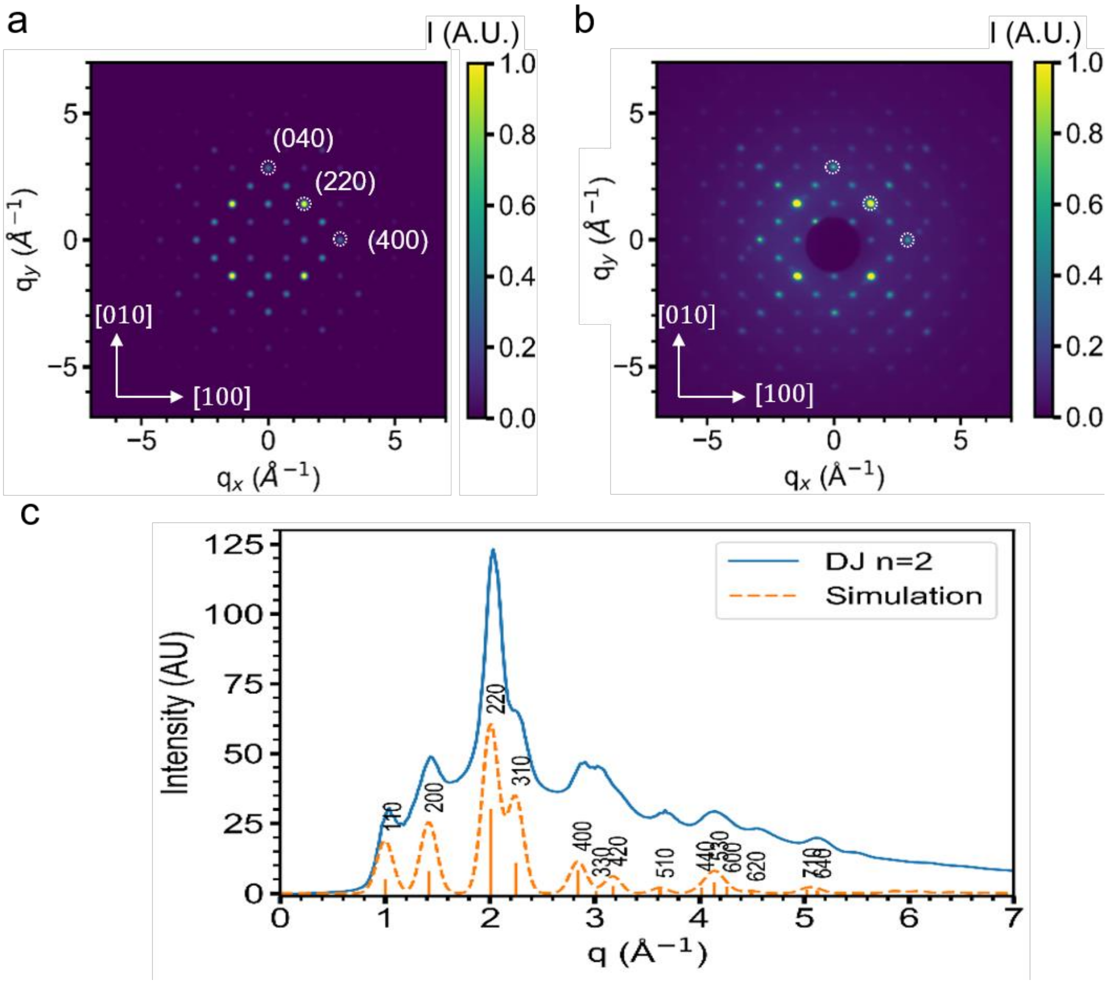

Fig. S2 | Simulated Diffraction Pattern & Indexing of DJ n=2 crystal. (a) Simulated Diffraction of DJ n=2 crystal, viewing from [001] direction. **(b)** Static Diffraction of DJ n=2, showing same q-range as the simulated one in Fig. S2a. All the Bragg peaks are well-identified. **(c)** Angular-integrated diffraction of DJ n=2, showing both experimental (blue solid line) and simulated (orange dashed line) plots, as well as Indexing of Bragg peaks (hk0).

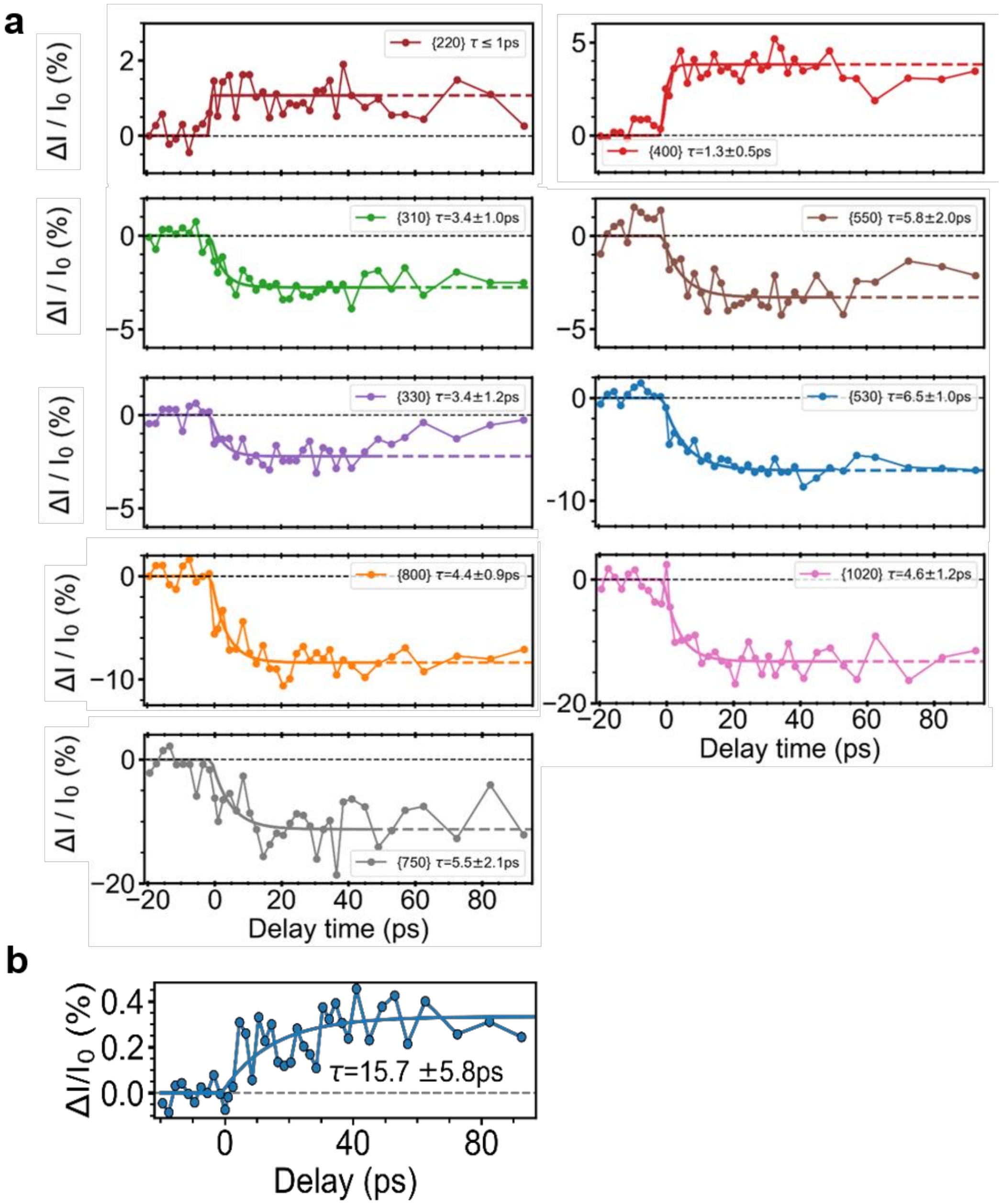

Fig. S3 | Time traces of selected Bragg peak families in DJ n=2 crystal. (a) Time traces of Bragg peaks intensities of {220}{400} {310} {330} {1020} {550} {530} {800} and {750} for DJ n=2 crystal. Errors of time constants are defined as one standard deviation errors estimated from the variance of the fitting parameters from least-squares fitting. The statistics of {220} is not good enough be fitted with a reasonable time constant. We estimate the time scale to be ≤1ps limited by temporal step size. **(b)** Dynamic plots of the total integrated diffuse scattering intensities between Bragg peaks.

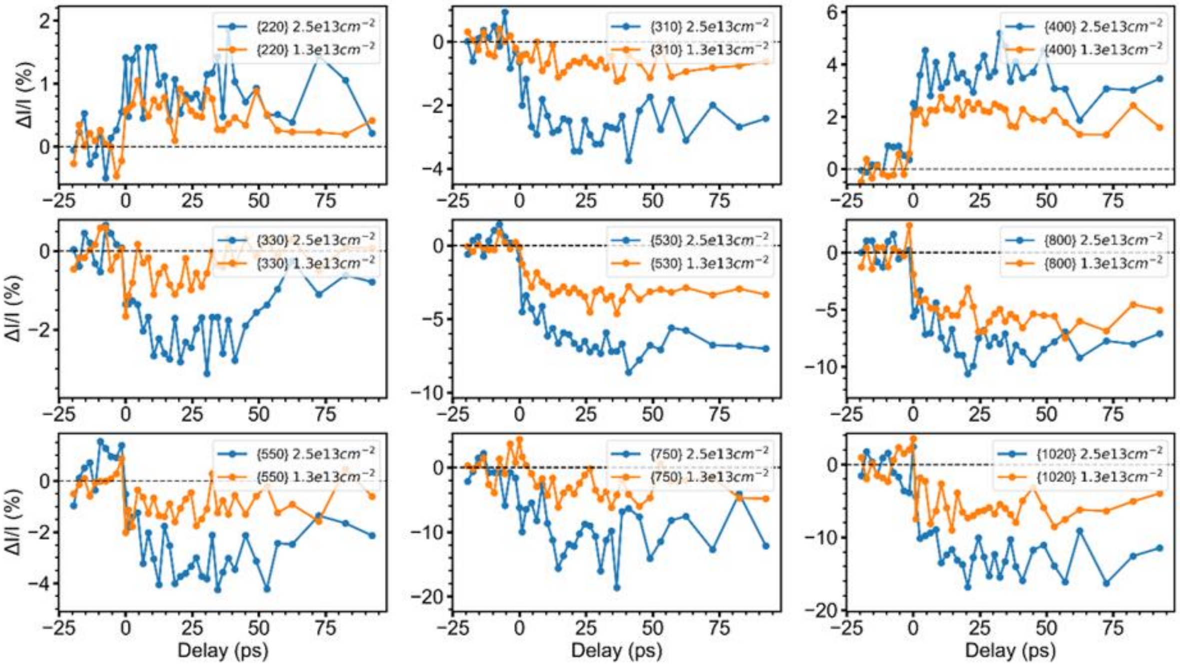

Fig. S4 | Fluence dependence for selected Bragg peaks in DJ n=2 crystal.

Time traces of Bragg peaks intensities of {220}{310} {400} {330} {530} {800} {550} {750} and {1020} for DJ n=2 crystal under 2 laser fluences: 1mJ/cm^2 (orange) and 2mJ/cm^2 (blue), corresponding to injected carrier density of 1.3×10^{13}cm^{-2} and 2.5×10^{13}cm^{-2}, respectively.

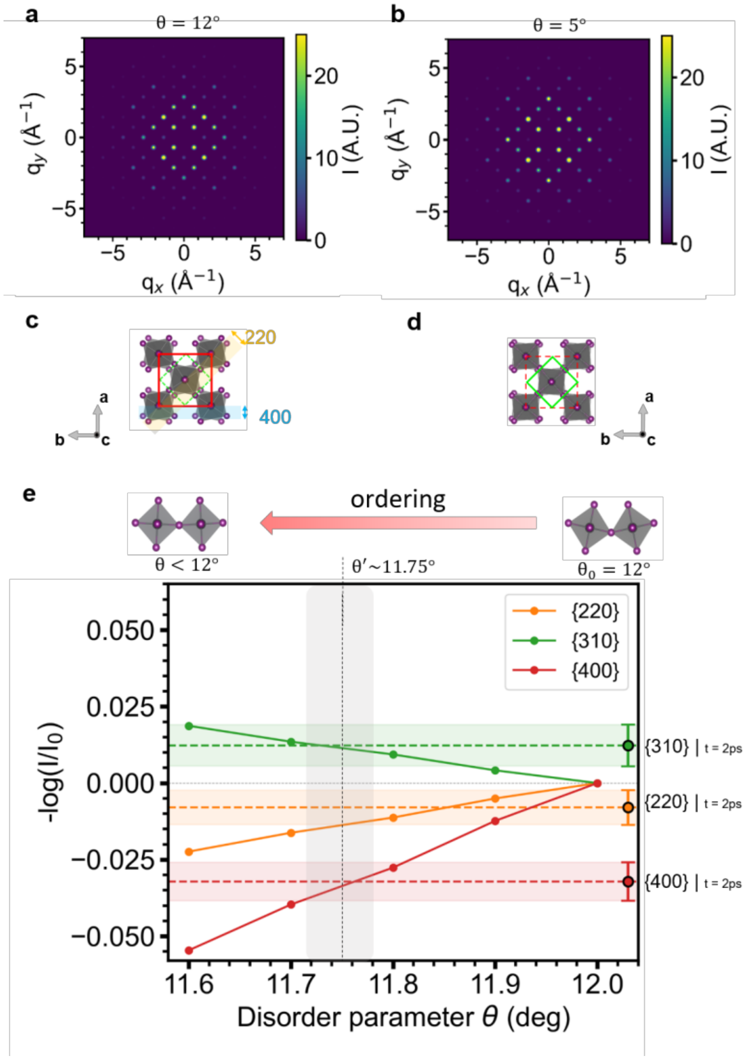

Fig. S5 | Simulated Diffraction Patterns with tuned antiferro-distortion. (a) Simulated Diffraction of DJ n=2 at rest with intrinsic antiferro-distortion ($\theta=12^{\circ}$). **(b)** Simulated Diffraction of DJ n=2 with reduced antiferro-distortion ($\theta=5^{\circ}$). **(c)(d)** Corresponding schematics of distorted ($\theta=12^{\circ}$) and less distorted phase ($\theta<12^{\circ}$), respectively. **(e)** Simulated logarithmic intensity change ($-\log(I/I_0)$) for selected Bragg peaks as a function of disorder parameter θ, shown for {220} {310} and {400} peaks (orange, green, and red solid lines), respectively. Compared with experimental data (DJ n=2, 2.6×10^{13} cm^{-2}) at t=2ps (scattered points at right), the optimal change of disorder parameter is estimated to be $\Delta\theta \sim 0.25^{\circ}$ (regime indicated in gray shadow).

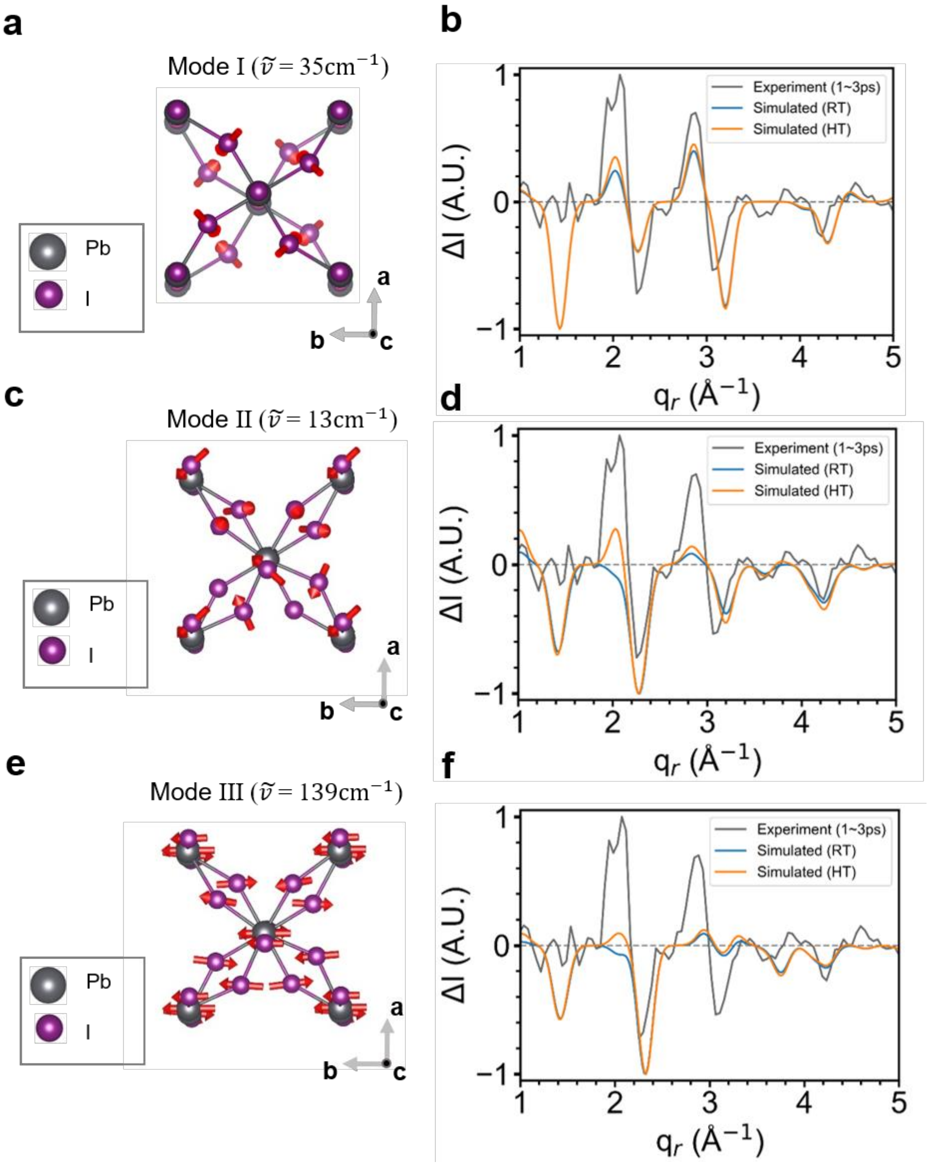

Fig. S6 | Examples of calculated antiferro-distortive phonon modes candidates in DJ n=2 crystal. (a)(c)(e) Schematic illumination of calculated normal modes (I, II and III respectively) acquired from phonon simulation (cations are neglected for visualization). The calculated wavenumbers are 35, 13, 139cm^{-1}, respectively. The directions of the atomic displacements are indicated with red arrows, suggesting a modulation of antiferro-distortions. **(d)(e)(f)** Simulated changes of electron diffraction plots for normal mode I, II and III respectively, estimated under room temperature (RT, blue solid line) and high temperature (HT, orange solid line) regimes. These simulated plots are compared with differential diffraction plot from UED experiment (1-3 ps, gray solid line), showing consistent peak increase at (220) and (400).

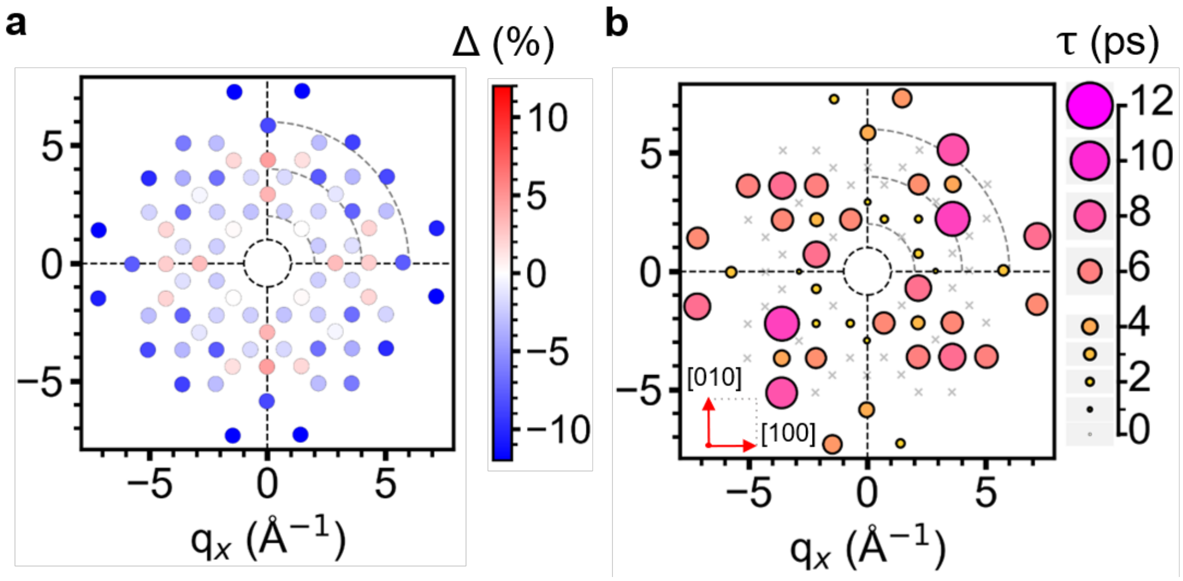

Fig. S7 | Scatter plots of fitted intensity change and time constants of DJ n=2 crystal. (a) Scatter plots of fitted intensity change (Δ (%)) of the Bragg peaks (hk0). Each Bragg peak (hk0) is averaged with (-h-k0) based on point symmetry. **(b)** Scatter plots of fitted time constant of the Bragg peaks, represented in both color scale and circle size (small and orange circles for short time, and large and pink circles for long time). ‘x’ markers stand for the Bragg peaks that cannot be well fit.

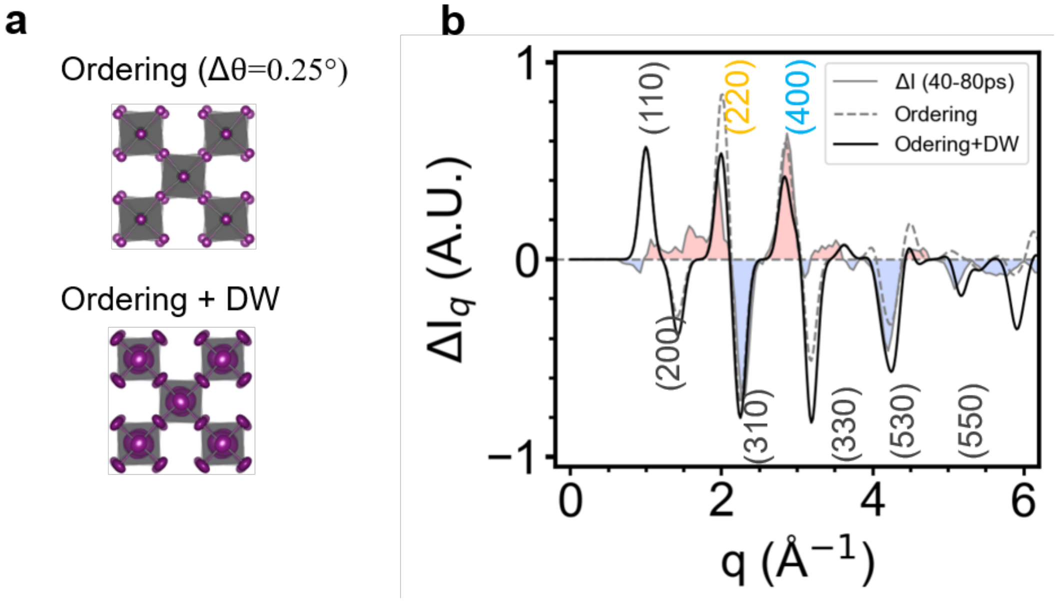

Fig. S8 | Simulation of total UED response of DJ n=2 crystal. (a) Simulated crystal structure (top view) for different simulation methods: lattice ordering by reducing distortion angle (top), and additional disorder involving all atoms (bottom). **(b)** Angular integrated differential diffraction plot, averaged between 40-80 ps (gray solid line and shadow), compared with the simulated response with only considering lattice ordering (gray dashed) and both ordering and Debye-Waller effect (black solid line). The experimental intensity around the (110) peak is partially blocked.

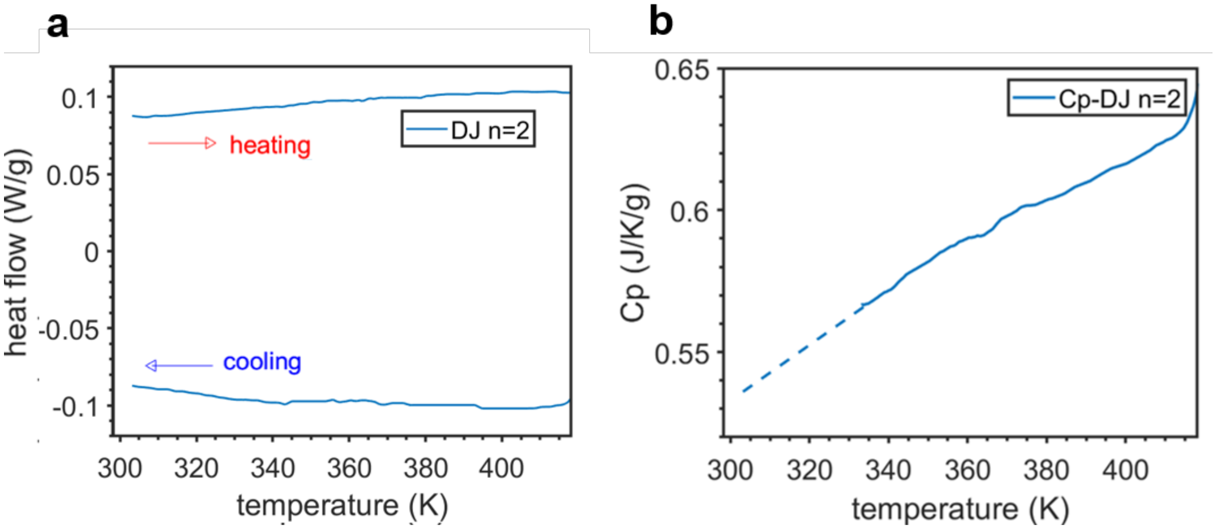

Fig. S9 | Differential scanning calorimetry (DSC) of DJ n=2 crystal. (a) DSC curve of DJ n=2 single crystals from room temperature to 150°C. **(b)** Calculated specific heat capacity (Cp) from DSC.

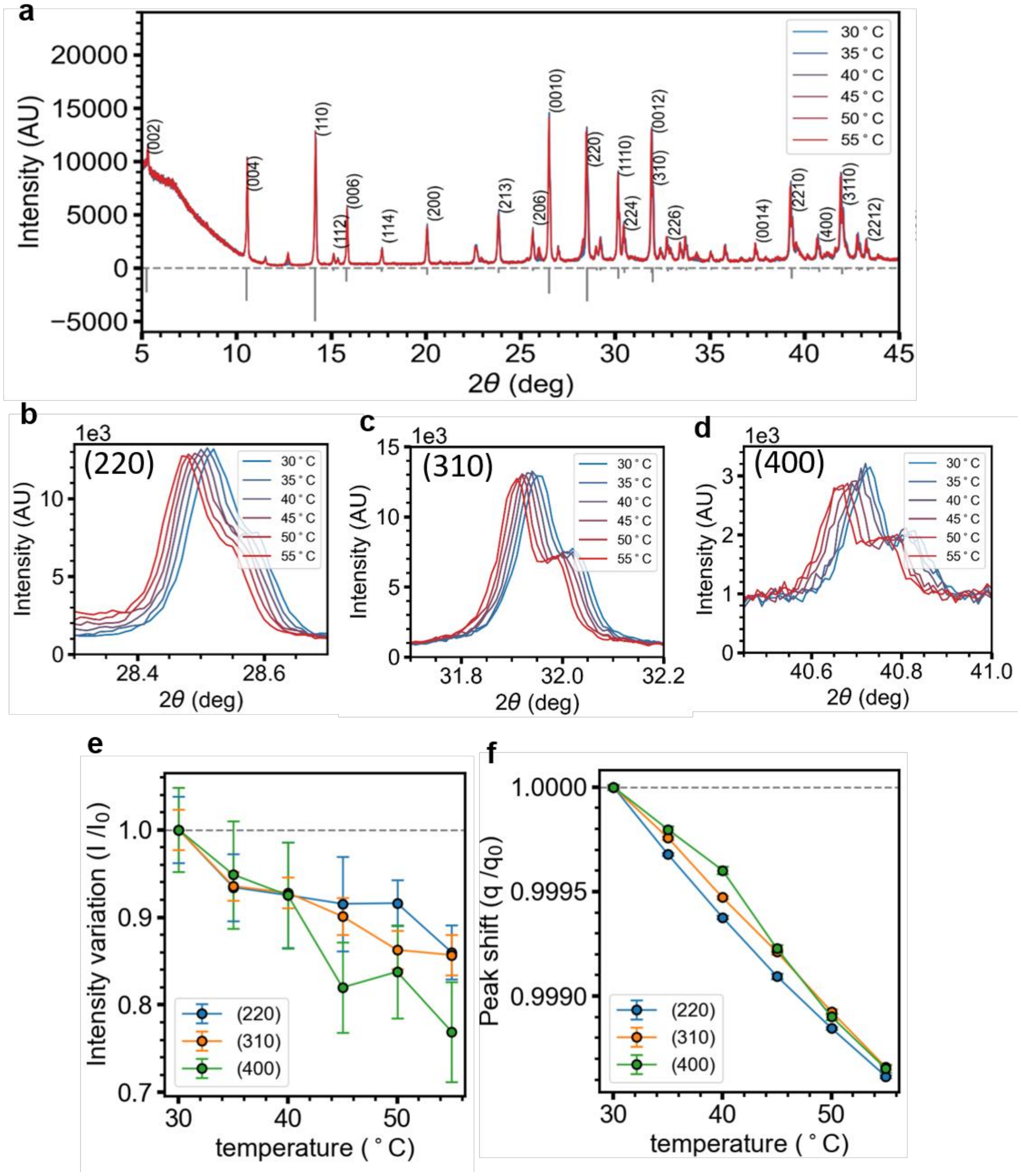

Fig. S10 | Temperature dependent XRD of DJ n=2 crystal. (a) Temperature dependent XRD from 30°C to 55°C. Simulated Bragg peak locations for DJ n=2 are indicated in vertical gray solid lines. **(b)(c)(d)** Zoomed-in XRD plots at in-plane peaks (220) (310) and (400) respectively, showing global shifting of peak locations (thermal expansion) and slight intensity decreases over temperature. **(e)** Analysis of relative intensity variation (I/I_0) and **(f)** relative peaks shift (q/q_0) for (220), (310) and (400) Bragg peaks. Error bars show the one standard deviation errors computed from the variance of the fitting parameters from least-squares fitting.

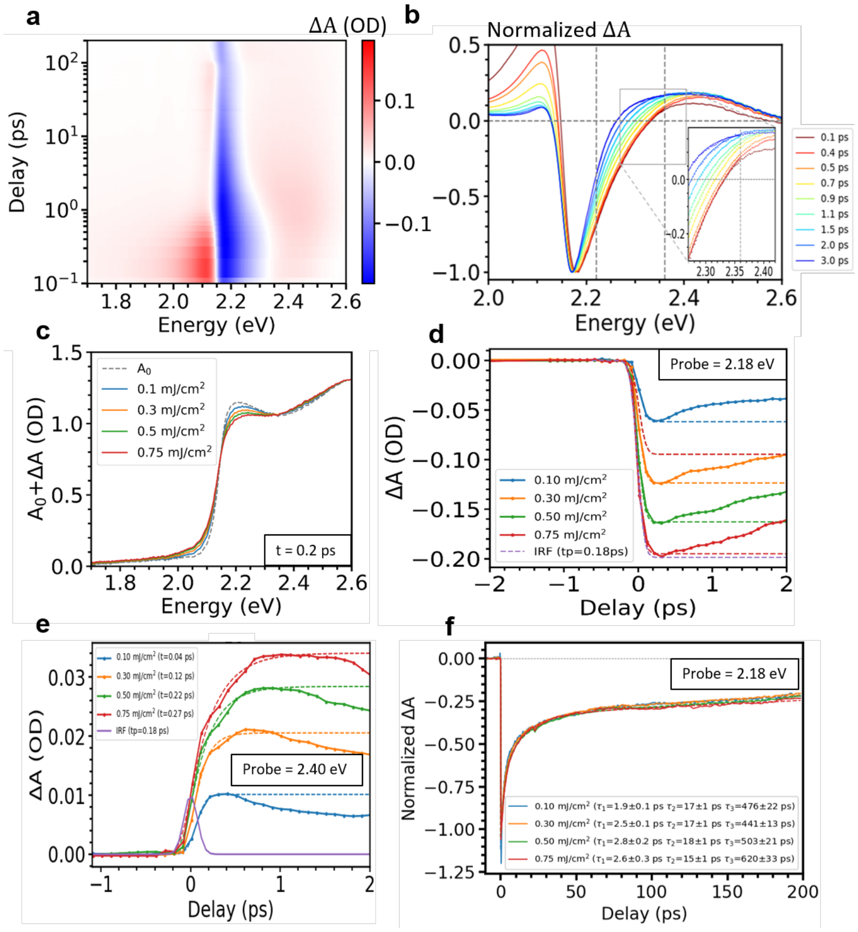

Fig. S11 | Transient absorption spectroscopy for DJ n=2 crystal. (a) Pseudo color representation of transient absorbance (Δ OD) as function of delay time, under 0.75mJ/cm^2. **(b)** Normalized TA spectra. The bleach amplitude at 2.18 eV is normalized to -1. High energy tails are fitted by Boltzmann distribution (black solid lines) to extract carrier temperature (shown in Fig. 3d). **(c)** Absolute absorption at various fluences, showing almost complete bleaching of exciton resonance. **(d)** Ultrafast bleaching ($\tau \leq 0.18$ ps) of exciton resonance at 2.18 eV, indicating fast ground state exciton bleaching after above-band excitation. **(e)** Evolution of TA dynamics at 2.40eV. The rise time is fitted with single exponential curve convolved with IRF (purple solid line), giving a rough estimation of carrier thermalization time. **(f)** Normalized exciton dynamics at 2.18eV, showing a long delay time (τ_3~10^2ps), suggesting a high density of electron-hole plasma still bleaches the exciton resonance at long time over 100-200ps. Fitting errors are estimated by the one standard deviation errors computed from the variance of the fitting parameters from least-squares fitting.

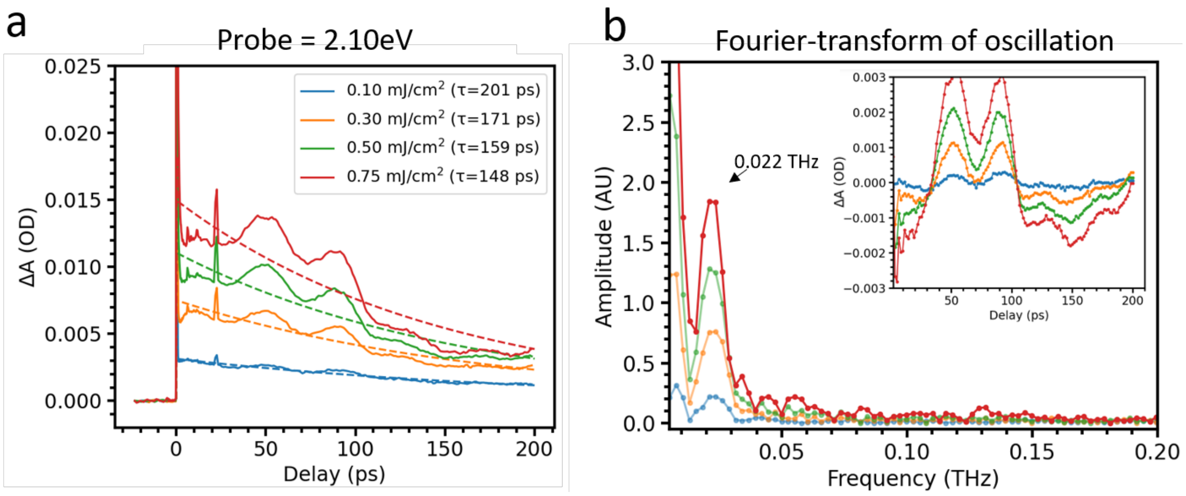

Fig. S12 | Observations of coherent acoustic phonon in DJ n=2 and frequency analysis. (a) TA decay of probed at 2.10eV, showing oscillatory components with period T~45ps. **(b)** Extraction of the oscillation (inset) and frequency domain analysis. Frequency below 0.0005THz is discarded due to the limited window in temporal domain (≤ 200 ps).

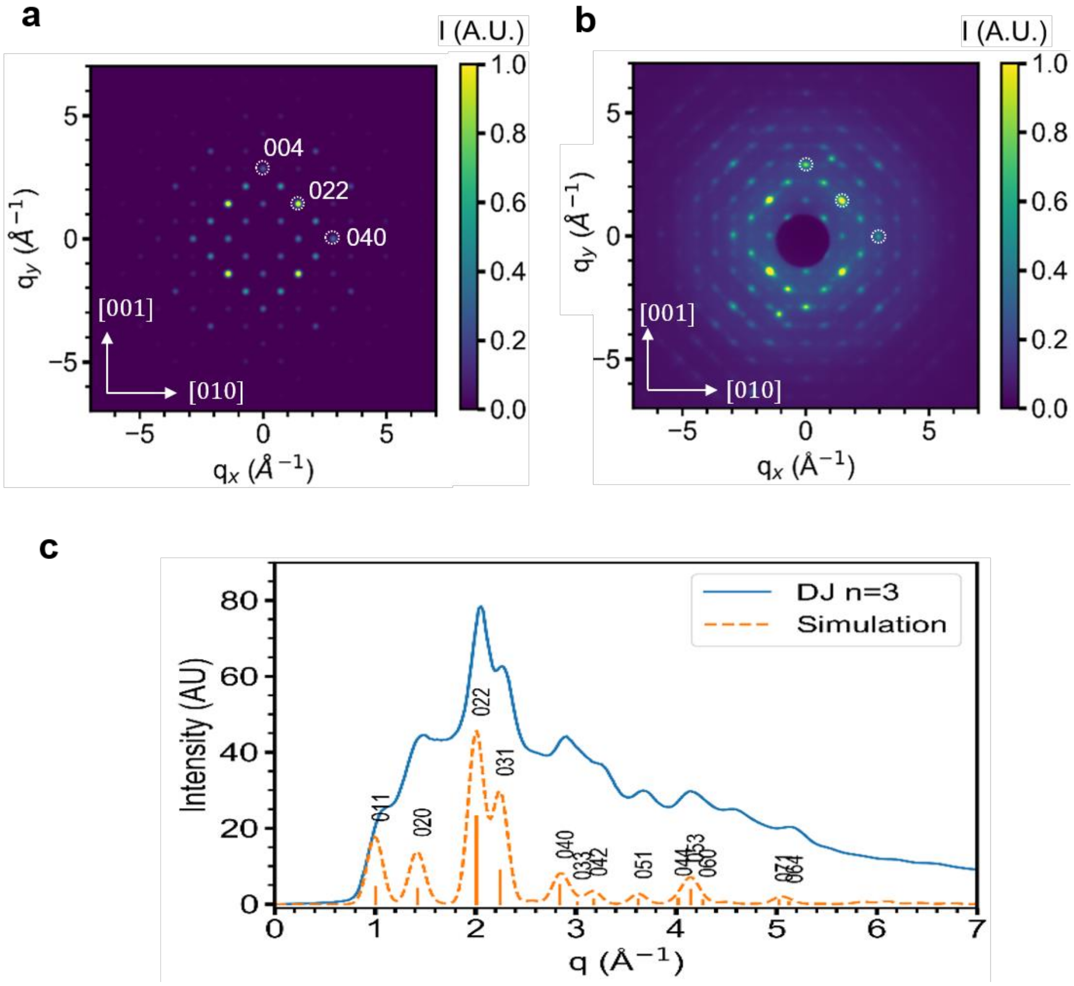

Fig. S13 | Simulated Diffraction Pattern & Indexing of DJ n=3 crystal.

(a) Simulated Diffraction of DJ n=3, viewing from [100] direction. **(b)** Static Diffraction of DJ n=3, showing same q-range as the simulated one in Fig. S13a. All the Bragg peaks are well-identified. **(c)** Angular-integrated diffraction of DJ n=3, showing both experimental (blue solid line) and simulated (orange dashed line) plots, as well as Indexing of Bragg peaks (0hk).

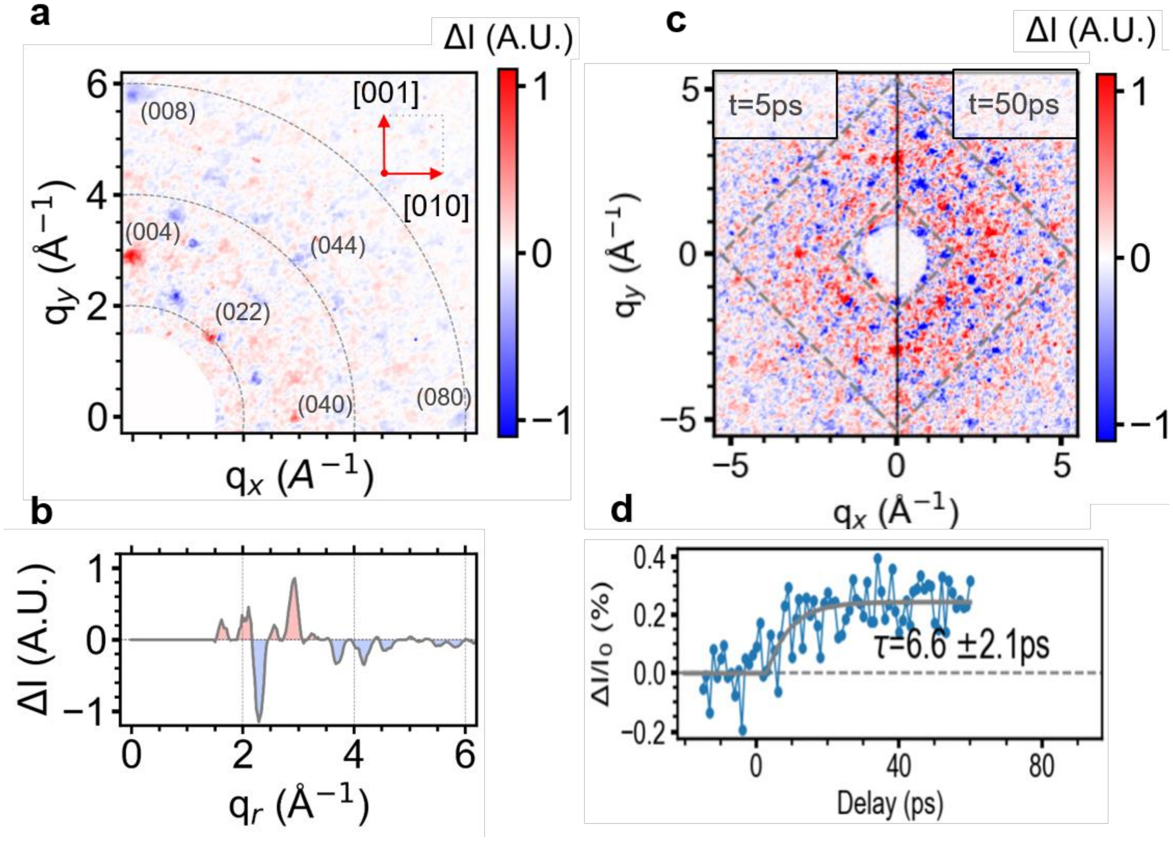

Fig. S14 | Differential diffraction patterns of DJ n=3. (a) Differential diffraction pattern (20-40ps) for DJ n=3, showing similar response as DJ n=2, including the positively-changing peaks (040), (022) and (004). **(b)** Angular-integrated differential diffraction (20-40ps) for DJ n=3. **(c)** Differential diffraction pattern at 5ps (left) and 50ps (right). The increasing red colors in between the peaks correlate to the diffuse scattering intensities. **(d)** Time traces of the integrated diffuse scattering intensities integrated with the two squares in **(c).** Fitting errors are estimated by the one standard deviation errors computed from the variance of the fitting parameters from least-squares fitting.

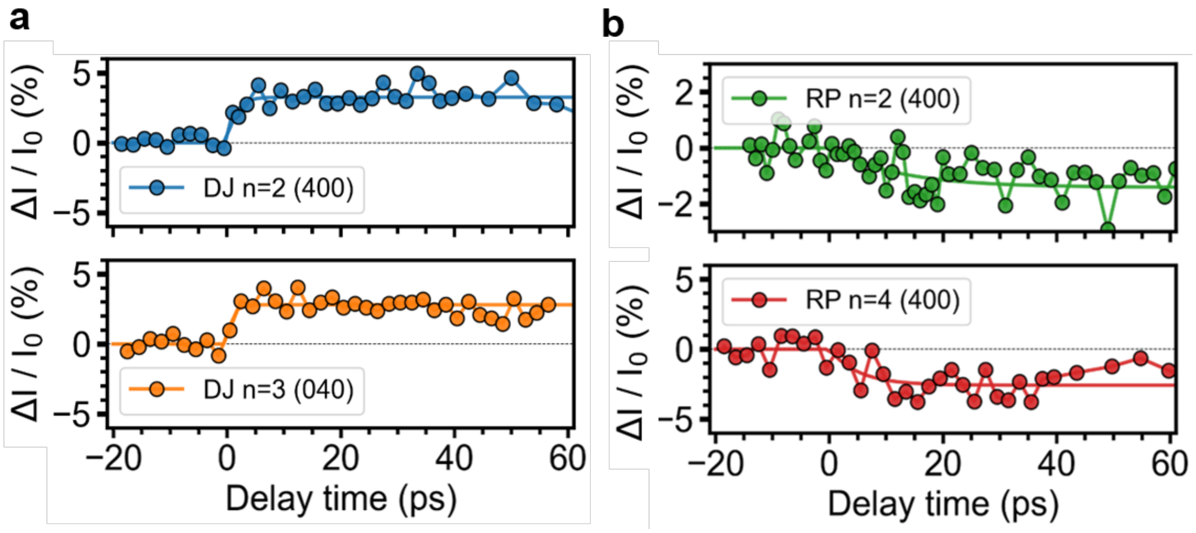

Fig. S15 | Comparison of time traces of selected Bragg peaks in 2D perovskites. (a) Time traces of DJ n=2 (400) (blue) and DJ n=3 (040) (orange) peak. Both peaks show a rapid increase in intensity. The rise-time constant fitted to be τ~1.3 ps (DJ n=2, blue solid line) and τ~0.9 ps (DJ n=3, orange solid line) respectively. **(b)** Time traces of RP n=2 (400) (green) and RP n=4 (400) (red) peak. Both peaks show a slower increase in intensity variations.

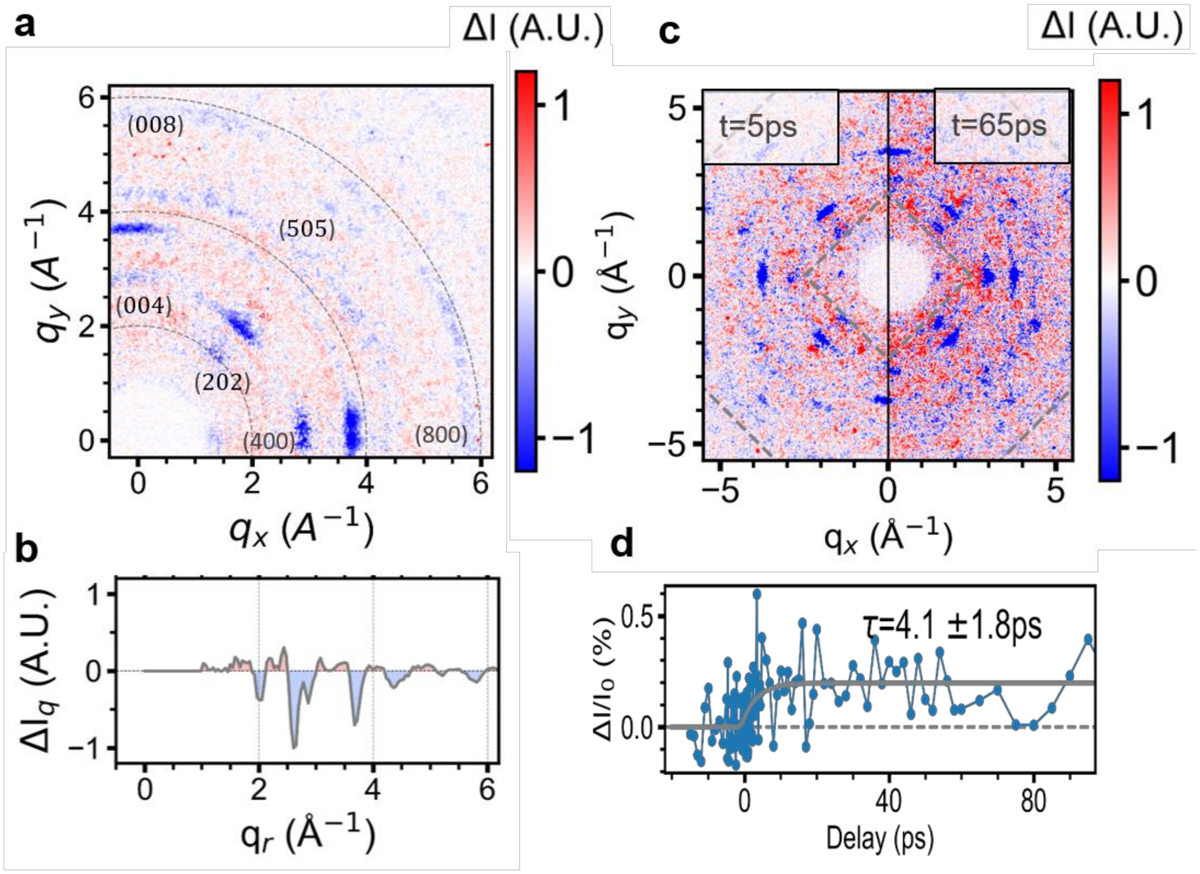

Fig. S16 | Differential diffraction patterns of RP n=2. (a) Differential diffraction pattern (15-40ps) for RP n=2, showing different response than DJ samples where no peaks increasing observed. **(b)** Angular-integrated differential diffraction (15-40ps) for RP n=2. **(c)** Differential diffraction pattern at 2ps (left) and 65ps (right). The increasing red colors in between the peaks correlate to the diffuse scattering intensities. **(d)** Time traces of the integrated diffuse scattering intensities integrated in-between the two squares in **(c)** (dashed line). Fitting errors are estimated by the one standard deviation errors computed from the variance of the fitting parameters from least-squares fitting.

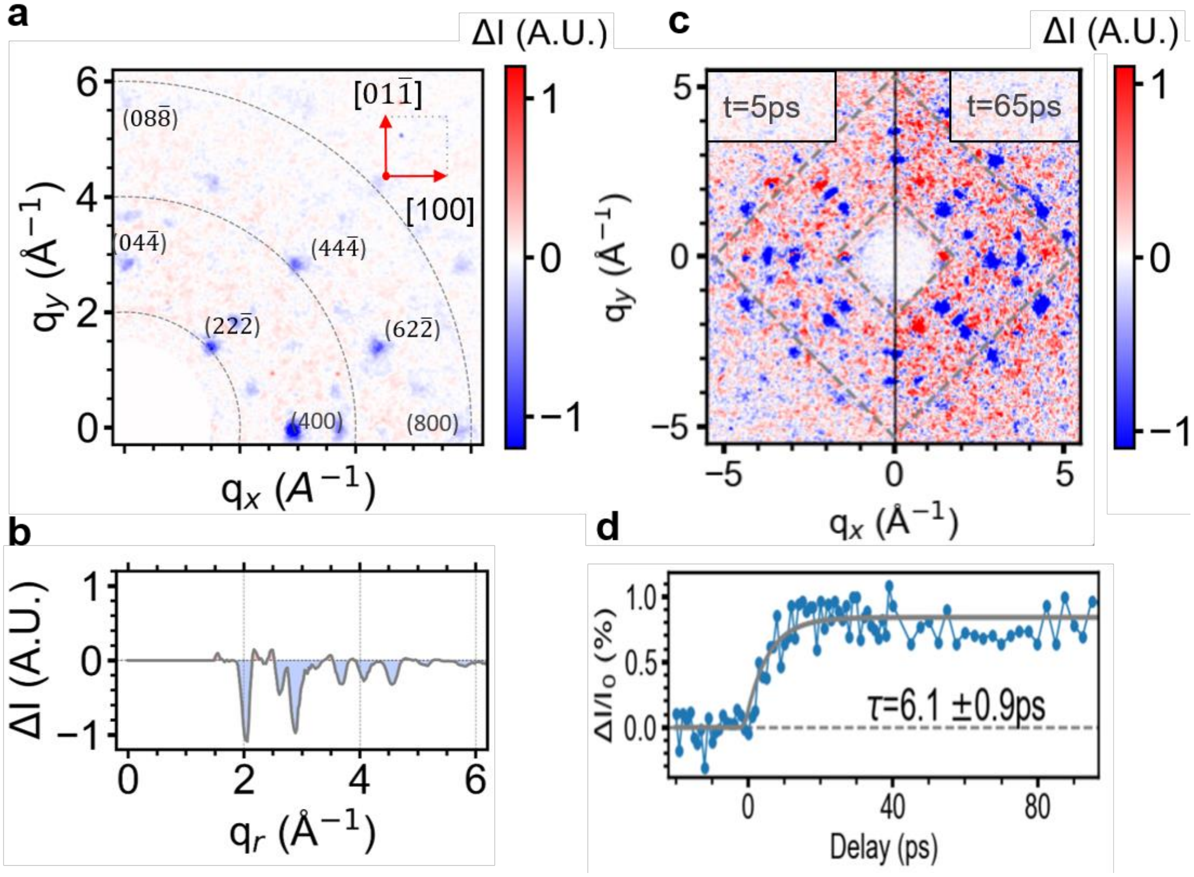

Fig. S17 | Differential diffraction patterns of RP n=4. (a) Differential diffraction pattern (20-40ps) for RP n=4, showing different response than DJ samples where no peaks increasing observed. **(b)** Angular-integrated differential diffraction (20-40ps) for RP n=4. **(c)** Differential diffraction pattern at 5ps (left) and 65ps (right). The increasing red colors in between the peaks correlate to the diffuse scattering intensities. **(d)** Time traces of the integrated diffuse scattering intensities integrated with the two squares in **(c).** Fitting errors are estimated by the one standard deviation errors computed from the variance of the fitting parameters from least-squares fitting.

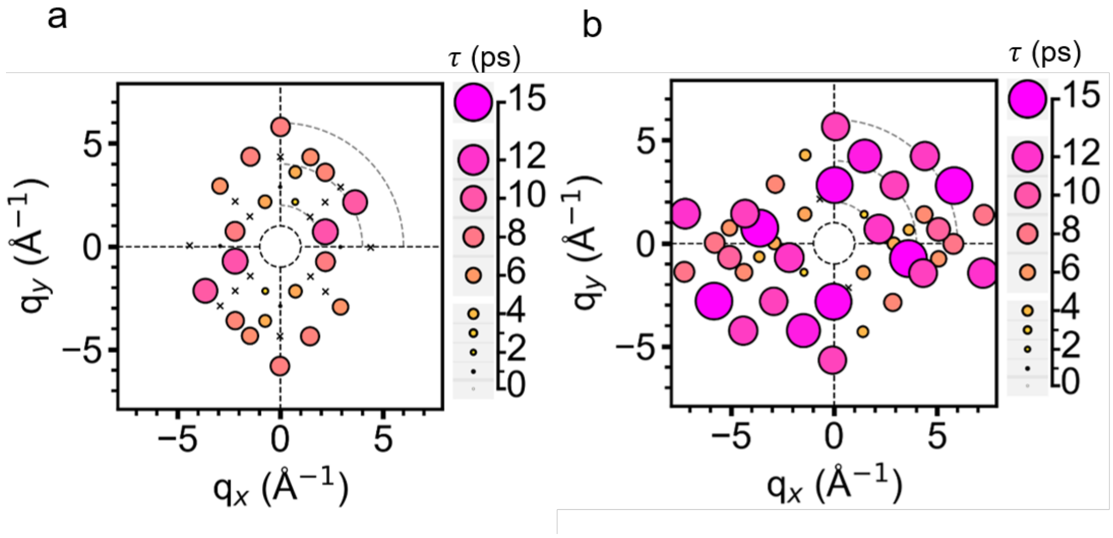

Fig. S18 | Time response comparison of different samples. Scatter plots of time constants (τ) of **(a)** DJ n=3 and **(b)** RP n=4 are shown. All the time constants are extracted from single exponential time fitting of Bragg peaks (averaged within each pair (hk0) and (-h-k 0)).

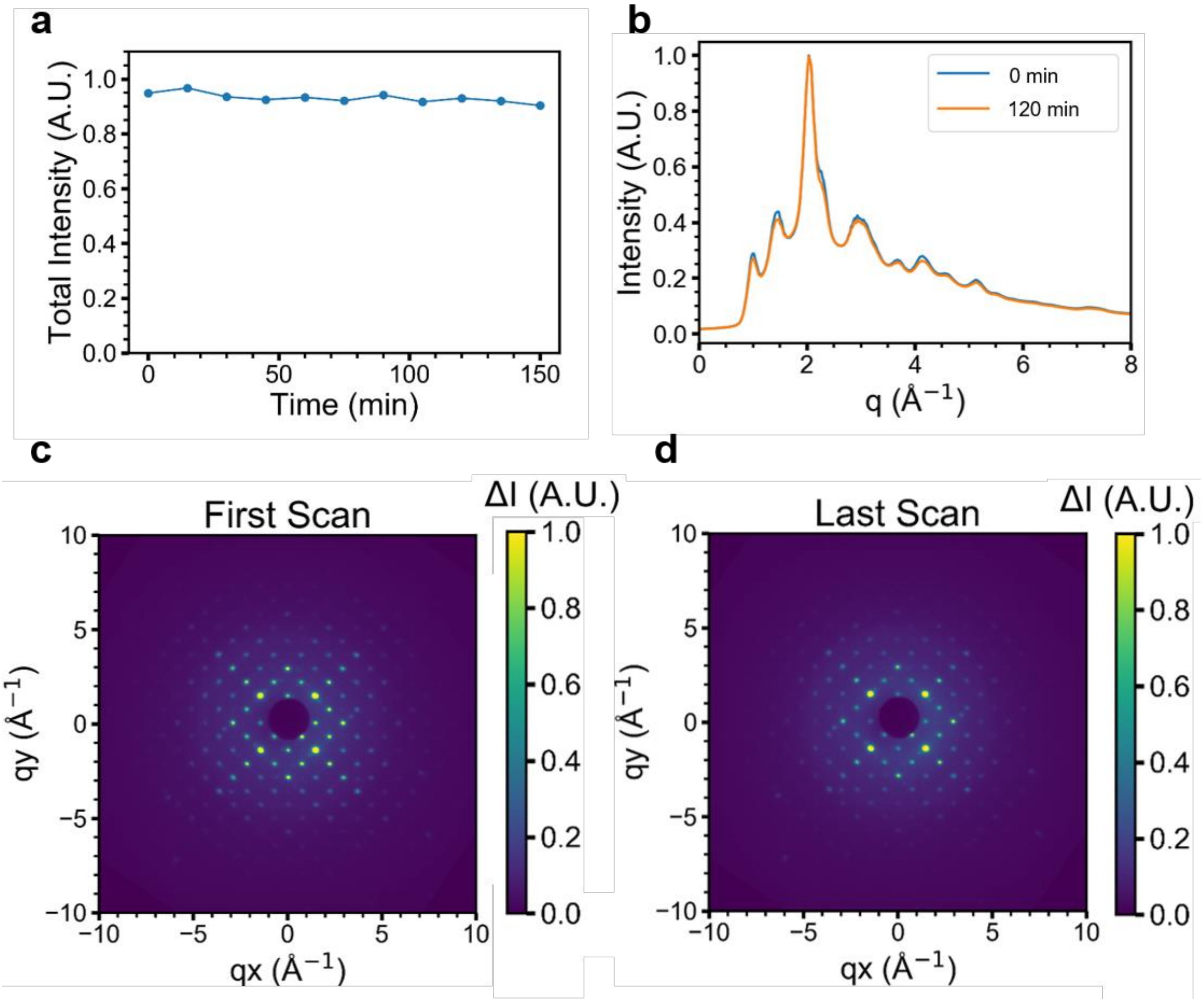

Fig. S19 | Time Evolution of diffraction intensity of DJ n=2 crystal. (a) Total electron diffraction intensity during UED measurements over 150mins. **(b)** Azimuth integrated plot of diffraction patterns taken at 0 min (blue) and 120mins (orange) after during the UED run. **(c)(d)** Diffraction images of **(c)** first and **(d)** last scan.

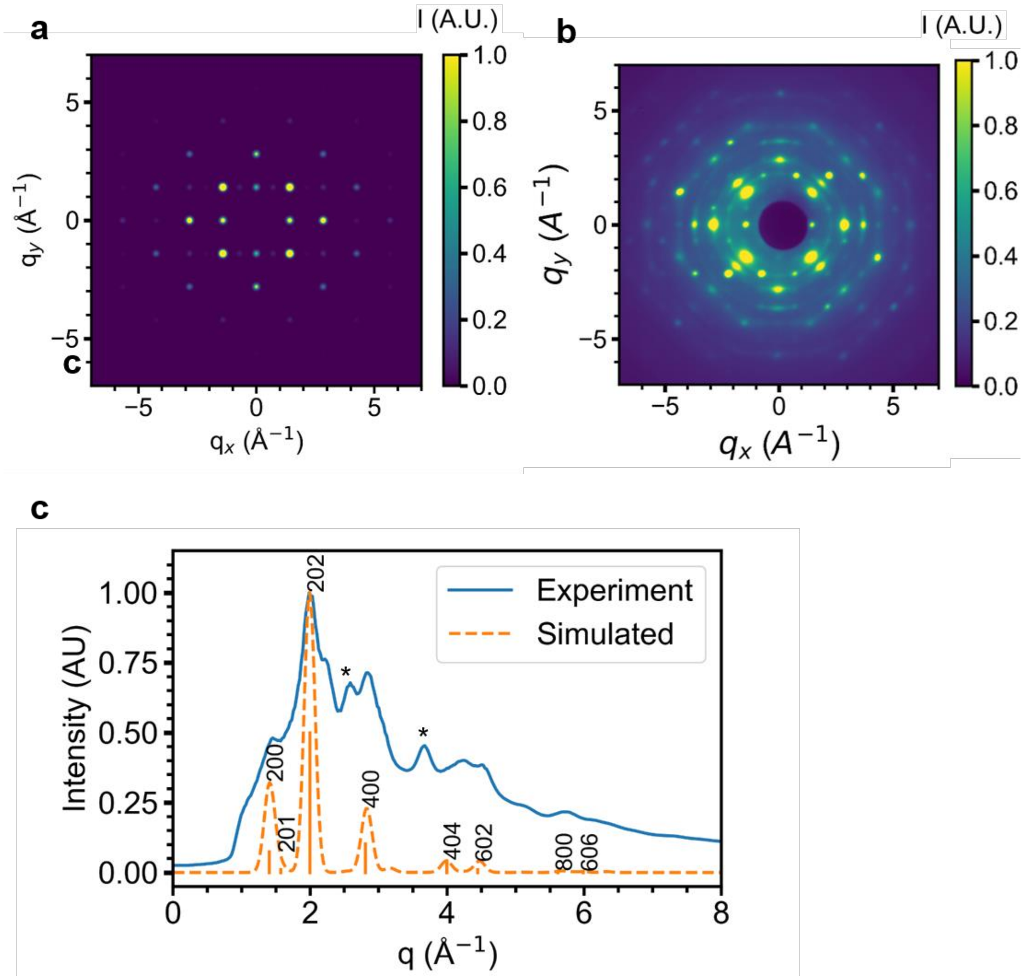

Fig. S20 | Simulated Diffraction Pattern & Indexing of RP n=2 crystal.

(a) Simulated Diffraction of DJ n=2, viewing from [010] direction. **(b)** Static Diffraction of RP n=2, showing same q-range as the simulated one in Fig. S20a. **(c)** Angular-integrated diffraction of RP n=2, showing both experimental (blue solid line) and simulated (orange dashed line) plots, as well as indexing of Bragg peaks (0hk).

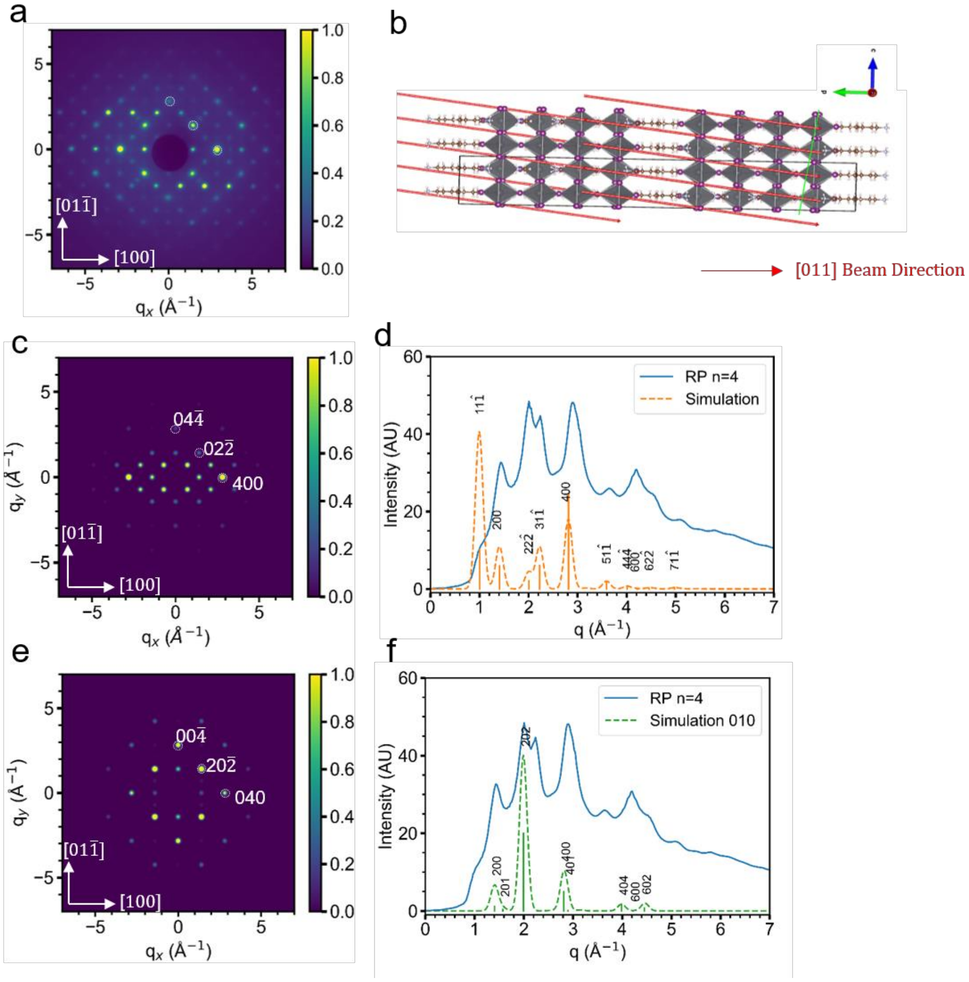

Fig. S21 | Simulated Diffraction Pattern & Indexing of RP n=4 crystal. (a) Static Diffraction patterns of RP n=4. **(b)** Schematics of RP n=4 and indication of [011] direction (red arrows). **(c)** Simulated Diffraction of RP n=4 along [011] direction. **(d)** Angular-integrated diffraction of RP n=4 viewing at [011], showing both experimental (blue solid line) and simulated (orange dashed line) plots, as well as Indexing of Bragg peaks. **(e)** Simulated Diffraction of RP n=4 along [010] direction, showing a mismatch with experimental patterns. **(f)** Angular-integrated diffraction of RP n=4 viewing at [010], showing both experimental (blue solid line) and simulated (green dashed line) plots, as well as Indexing of Bragg peaks.

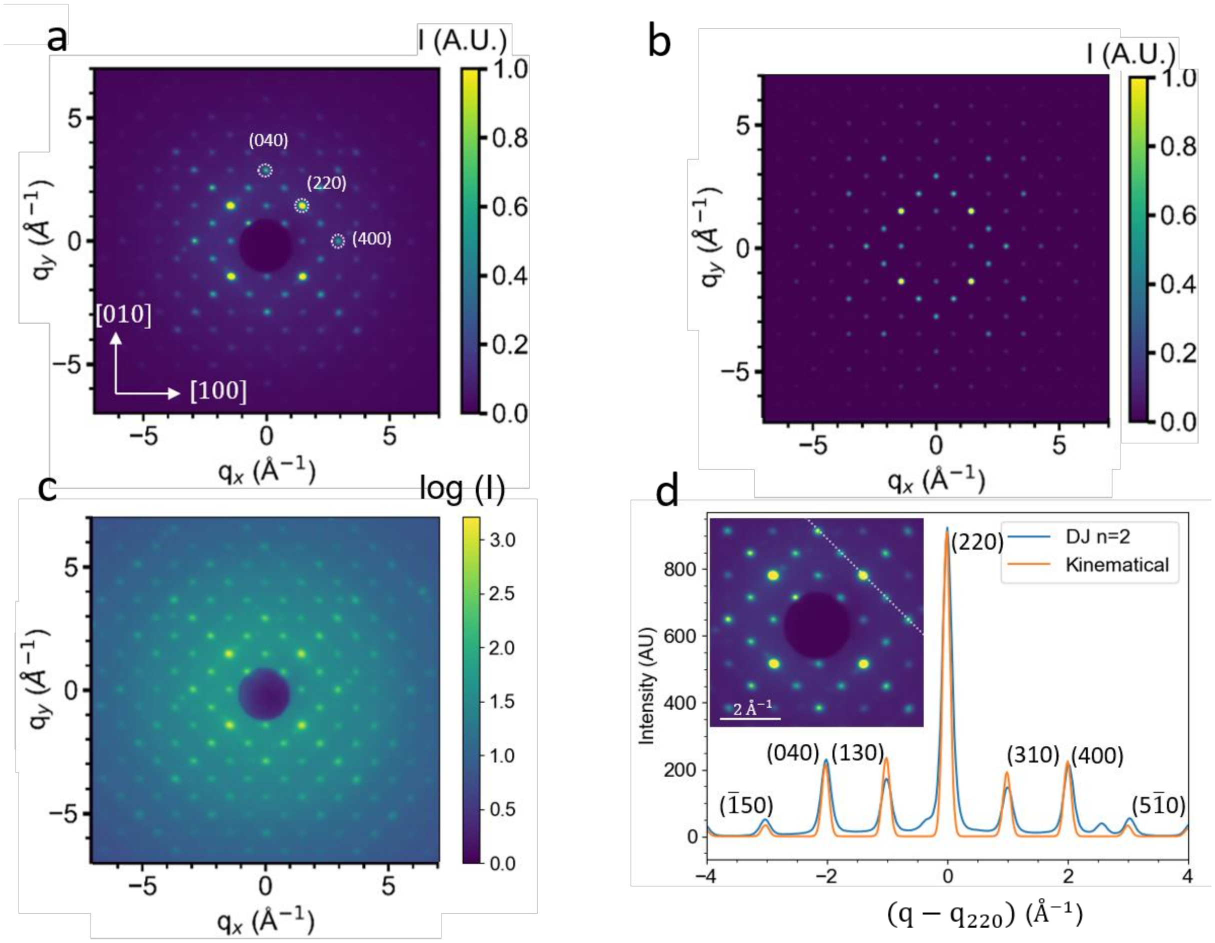

Fig. S22 | Comparison of the diffraction pattern of DJ n=2 with kinematical theory. (a) Static diffraction pattern of DJ n=2 crystal. **(b)** Simulated diffraction pattern with Kinematical scattering along c direction, computed from 4×4 supercell. **(c)** Logarithmic scale of the DJ n=2 diffraction pattern from (a), showing individual isolated Bragg peaks without Kikuchi lines. **(d)** Comparison of the linecuts of diffraction pattern along (040)-(040) direction (indicted by white dashed line in inset), showing consistent intensity distributions between experimental diffractions (blue) and the ones from kinematic theory (orange).

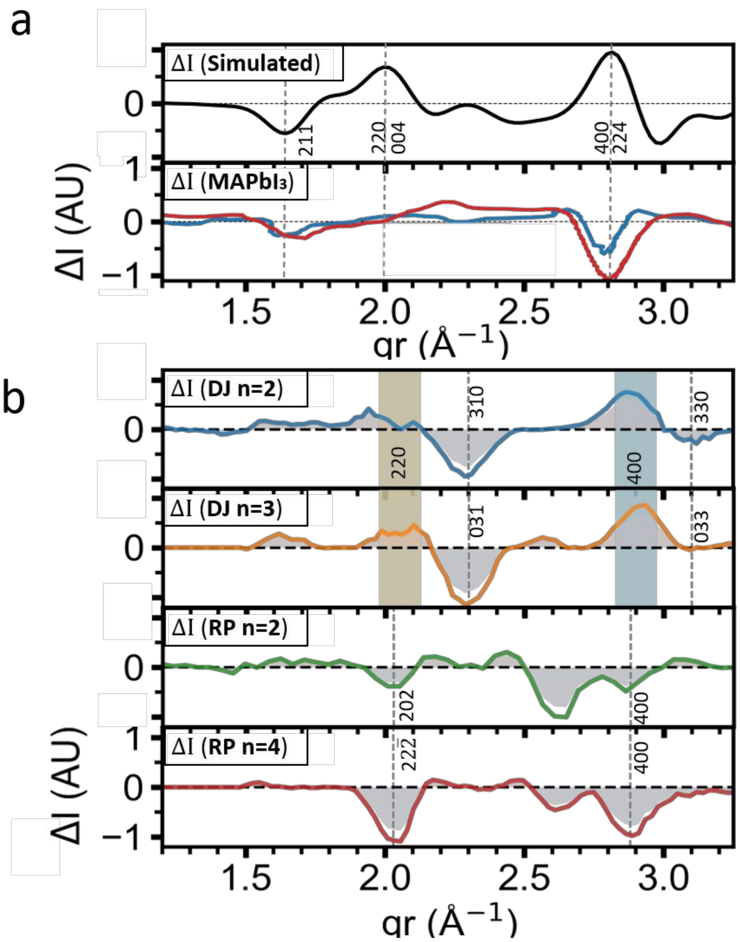

Fig. S23 | Comparison of the angular-integrated diffraction of MAPbI3, with 2D DJ and RP perovskites. (a) The simulated differential diffraction pattern (black) is computed assuming a complete reduction of the antiferro-distorsion present in the tetragonal phase of MAPbI3, leading to a cubic lattice. The Bragg indices are assigned for the initial tetragonal structure. The simulation is compared to the experimental differential diffraction curves of MAPbI3 for delay time t=5ps (blue) and t=70ps (red) (Data extracted from Wu et al[1]). **(b)** Differential diffraction plots of 2D perovskites reported in this work (Fig. 4c in manuscript).

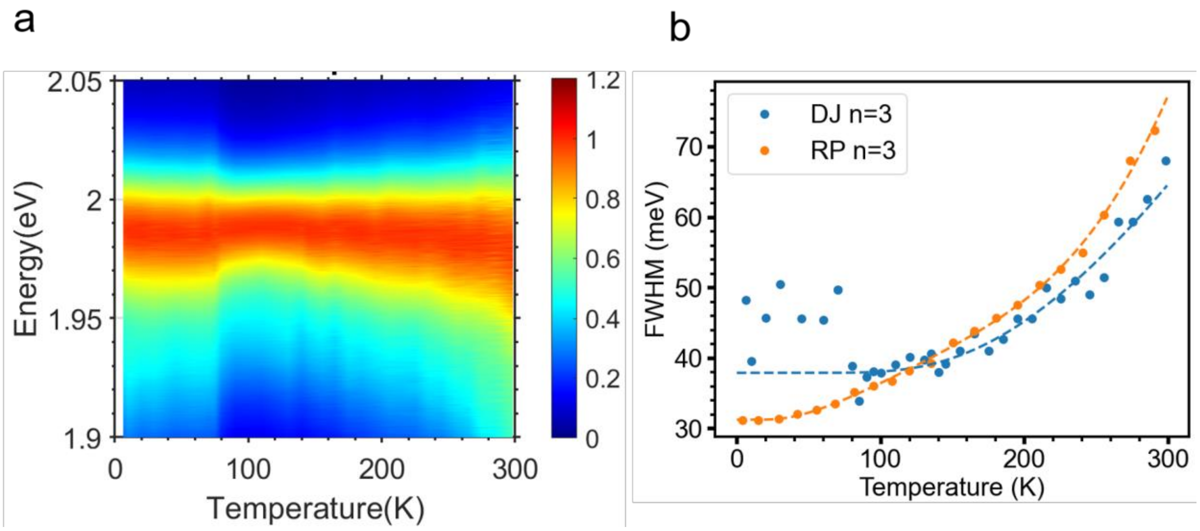

Fig. S24 | Temperature dependent PL on DJ and RP n=3 crystal. (a) Pseudo-colormap of PL as a function of temperature. **(b)** Extracted PL linewidth broadening, fitted with electron-LO phonon coupling model (dashed line).

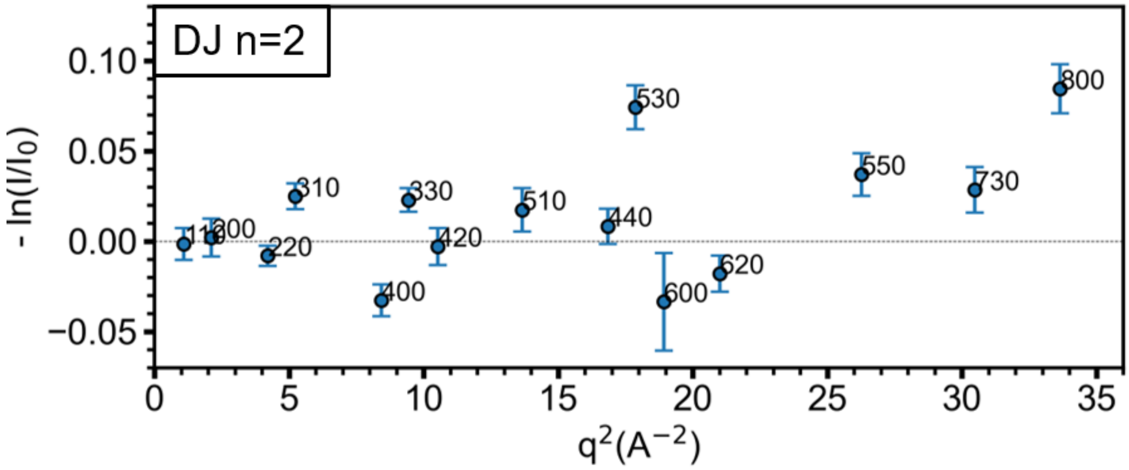

Fig. S25 | Semi-log plot of Bragg peaks intensity change as a function of q^2 for DJ n=2. Logarithmic plot of Bragg peaks total relative intensity change ($-\log(I/I_0)$) DJ n=2 under pump fluence energy of 2mJ/cm^2. Errors are estimated by the standard deviations of the intensity responses between 30 and 60ps (where quasi-equilibrium has been established for the Bragg peaks).

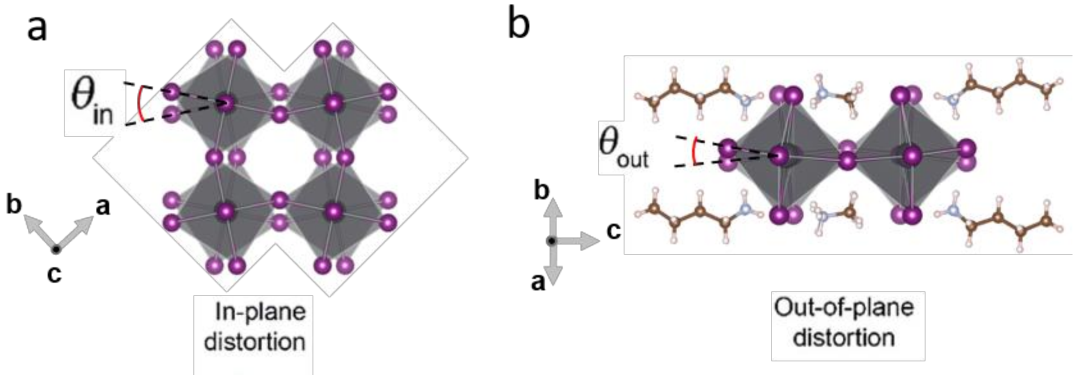

Fig. S26 | Illustration of in-plane and out-of-plane octahedral tilts. (a)(b) Definitions of the in-plane and out-of-plane octahedral tilts, respectively. A list of the octahedral tilts for measured perovskites is displayed in Table S2. The stacking axis of the 2D-HaPs is represented along c axis. The organics are not displayed in (a) for simplified visualization.

Supplementary Tables S1 - S2

Sample Name	DJ n=2	DJ n=3	RP n=2	RP n=4
Excitation Energy (eV)	3.1	3.1	3.1	3.1
Fluence (mJ/cm^2):	2	2.2	0.45	2.5
Crystal thickness (nm):	270	450	200	380
Optical density (at 3.1eV):	2.2	2.5	2.5	2.5
Carrier density (cm^{-2})	2.5×10^{13}	2.3×10^{13}	8.9×10^{12}	4.2×10^{13}

Table. S1 | Lists of experimental conditions of the measured samples: crystal thickness, excitation fluences and carrier densities. Sample thickness are estimated from the optical absorbance data in Fig. S1 for DJ n=2.

Sample Name	$\mathrm{(4AMP)Pb_2I_7}$ (DJ n=2)	$\mathrm{(4AMP)Pb_3I_{10}}$ (DJ n=3)	$\mathrm{(BA)_2PbI_2I_7}$ (RP n=2)	$\mathrm{(BA)_2PbI_4I_{13}}$ (RP n=4)	$\mathrm{MAPbI_3}$	$\mathrm{SrTiO_3}$ (< 1.5 K)	$\mathrm{KTaO_3}$
Crystal system	Monoclinic	Monoclinic	Orthorhombic	Orthorhombic	Tetragonal	Tetragonal	Cubic
Structural phase	2D - DJ	2D - DJ	2D - RP	2D - RP	3D	3D	3D
Tilt (in-plane) (°)	11.78	11.2	0.02	0.03	/	/	/
Tilt (out-of-plane) (°)	0.72	0.46	7.66	6.42	/	/	/
Tilt (tetragonal axis) (°)	/	/	/	/	8.15	~2	0
Reference	3	3	4	4	13	27	32

Table. S2 | List of interlayer octahedral tilts (order parameter θ) for halide and oxide perovskites. The values are extracted from the corresponding crystal structures at room temperature (except for T<1.5K for $SrTiO_3$). For 2D perovskites, the octahedral tilts with in-plane (along stacking axis) vs out-of-plane (perpendicular to stacking axis) directions are distinguished (see Fig. S26). For 3D perovskites, similar tilt is defined along tetragonal axis.

References

1. Wu, X. *et al.* Light-induced picosecond rotational disordering of the inorganic sublattice in hybrid perovskites. *Science Advances* **3**, e1602388 (2017).
2. Song, B. *et al.* Determination of Dielectric Functions and Exciton Oscillator Strength of Two-Dimensional Hybrid Perovskites. *ACS Materials Lett.* **3**, 148–159 (2021).
3. Mao, L. *et al.* Hybrid Dion–Jacobson 2D Lead Iodide Perovskites. *J. Am. Chem. Soc.* **140**, 3775–3783 (2018).
4. Stoumpos, C. C. *et al.* Ruddlesden–Popper Hybrid Lead Iodide Perovskite 2D Homologous Semiconductors. *Chem. Mater.* **28**, 2852–2867 (2016).
5. Lin, M.-F. *et al.* Ultrafast non-radiative dynamics of atomically thin MoSe 2. *Nature Communications* **8**, 1745 (2017).
6. Ghosh, D. *et al.* Charge carrier dynamics in two-dimensional hybrid perovskites: Dion–Jacobson vs. Ruddlesden–Popper phases. *Journal of Materials Chemistry A* **8**, 22009–22022 (2020).
7. Gong, X. *et al.* Electron–phonon interaction in efficient perovskite blue emitters. *Nature Materials* **17**, 550–556 (2018).
8. Quan, L. N. *et al.* Vibrational relaxation dynamics in layered perovskite quantum wells. *PNAS* **118**, (2021).
9. Morrison, V. R. *et al.* A photoinduced metal-like phase of monoclinic VO2 revealed by ultrafast electron diffraction. *Science* **346**, 445–448 (2014).
10. González Vallejo, I. *et al.* Observation of large multiple scattering effects in ultrafast electron diffraction on monocrystalline silicon. *Phys. Rev. B* **97**, 054302 (2018).
11. Park, I.-H. *et al.* Self-Powered Photodetector Using Two-Dimensional Ferroelectric Dion–Jacobson Hybrid Perovskites. *J. Am. Chem. Soc.* **142**, 18592–18598 (2020).

12. Li, J. *et al.* Cs2PbI2Cl2, All-Inorganic Two-Dimensional Ruddlesden–Popper Mixed Halide Perovskite with Optoelectronic Response. *J. Am. Chem. Soc.* **140**, 11085–11090 (2018).

13. Stoumpos, C. C., Malliakas, C. D. & Kanatzidis, M. G. Semiconducting Tin and Lead Iodide Perovskites with Organic Cations: Phase Transitions, High Mobilities, and Near-Infrared Photoluminescent Properties. *Inorg. Chem.* **52**, 9019–9038 (2013).

14. Williams, D. B. & Carter, C. B. *Transmission electron microscopy: a textbook for materials science*. (Springer, 2008).

15. Peng, L.-M., Ren, G., Dudarev, S. L. & Whelan, M. J. Robust Parameterization of Elastic and Absorptive Electron Atomic Scattering Factors. *Acta Cryst A* **52**, 257–276 (1996).

16. Peng, L.-M. Electron Scattering Factors of Ions and their Parameterization. *Acta Cryst A* **54**, 481–485 (1998).

17. Kirkland, E. J. *Advanced Computing in Electron Microscopy*. (Springer US, 2010). doi:10.1007/978-1-4419-6533-2.

18. scikit-ued: (ultrafast) electron diffraction tools — scikit-ued 2.1.12 documentation. https://scikit-ued.readthedocs.io/en/master/index.html.

19. Otto, M. R. *et al.* Mechanisms of electron-phonon coupling unraveled in momentum and time: The case of soft phonons in TiSe2. *Science Advances* **7**, eabf2810 (2021).

20. Price, M. B. *et al.* Hot-carrier cooling and photoinduced refractive index changes in organic–inorganic lead halide perovskites. *Nat Commun* **6**, 8420 (2015).

21. Richter, J. M. *et al.* Ultrafast carrier thermalization in lead iodide perovskite probed with two-dimensional electronic spectroscopy. *Nature Communications* **8**, 376 (2017).

22. Yang, Y. *et al.* Observation of a hot-phonon bottleneck in lead-iodide perovskites. *Nature Photonics* **10**, 53–59 (2016).

23. Thouin, F. *et al.* Phonon coherences reveal the polaronic character of excitons in two-dimensional lead halide perovskites. *Nature Materials* **18**, 349–356 (2019).

24. Schmitt-Rink, S., Chemla, D. S. & Miller, D. A. B. Theory of transient excitonic optical nonlinearities in semiconductor quantum-well structures. *Phys. Rev. B* **32**, 6601–6609 (1985).

25. Blancon, J.-C. *et al.* Scaling law for excitons in 2D perovskite quantum wells. *Nature Communications* **9**, 2254 (2018).

26. Ishihara, T., Takahashi, J. & Goto, T. Optical properties due to electronic transitions in two-dimensional semiconductors (${\mathrm{C}}_{\mathit{n}}$${\mathrm{H}}_{2\mathit{n}+1}$${\mathrm{NH}}_{3}$ ${)}_{2}$${\mathrm{PbI}}_{4}$. *Phys. Rev. B* **42**, 11099–11107 (1990).

27. Kiat, J. M. & Roisnel, T. Rietveld analysis of strontium titanate in the Müller state. *J. Phys.: Condens. Matter* **8**, 3471–3475 (1996).

28. Radha, S. K., Bhandari, C. & Lambrecht, W. R. L. Distortion modes in halide perovskites: To twist or to stretch, a matter of tolerance and lone pairs. *Phys. Rev. Materials* **2**, 063605 (2018).

29. Bruce, A. D. & Cowley, R. A. Lattice dynamics of strontium titanate: anharmonic interactions and structural phase transitions. *J. Phys. C: Solid State Phys.* **6**, 2422–2440 (1973).

30. Akbarzadeh, A. R., Bellaiche, L., Leung, K., Íñiguez, J. & Vanderbilt, D. Atomistic simulations of the incipient ferroelectric $\mathrm{K}\mathrm{Ta}{\mathrm{O}}_{3}$. *Phys. Rev. B* **70**, 054103 (2004).

31. Wright, A. D. *et al.* Electron–phonon coupling in hybrid lead halide perovskites. *Nature Communications* **7**, 11755 (2016).
32. KTaO3 Crystal Structure: Datasheet from “PAULING FILE Multinaries Edition – 2012” in SpringerMaterials (https://materials.springer.com/isp/crystallographic/docs/sd_1412930).